



CHALMERS
UNIVERSITY OF TECHNOLOGY

Formation of Complex Organic Molecules in Prestellar Cores: The Role of Nondiffusive Grain Chemistry

Downloaded from: <https://research.chalmers.se>, 2026-05-15 08:35 UTC

Citation for the original published paper (version of record):

Borshcheva, K., Fedoseev, G., Punanova, A. et al (2025). Formation of Complex Organic Molecules in Prestellar Cores: The Role of Nondiffusive Grain Chemistry. *Astrophysical Journal*, 990(2). <http://dx.doi.org/10.3847/1538-4357/adea73>

N.B. When citing this work, cite the original published paper.



Formation of Complex Organic Molecules in Prestellar Cores: The Role of Nondiffusive Grain Chemistry

Katerina Borshcheva^{1,2} , Gleb Fedoseev^{1,3,4} , Anna F. Punanova⁵ , Paola Caselli⁶ , Izaskun Jiménez-Serra⁷ , and Anton I. Vasyunin¹

¹Research Laboratory for Astrochemistry, Ural Federal University, Mira st. 19 Yekaterinburg, Russia

²Institute of Astronomy of the Russian Academy of Sciences, Pyatnitskaya str. 48 Moscow, Russia

³Xinjiang Astronomical Observatory, Chinese Academy of Sciences, Urumqi 830011, People's Republic of China

⁴Xinjiang Key Laboratory of Radio Astrophysics, Urumqi 830011, People's Republic of China

⁵Onsala Space Observatory, Chalmers University of Technology, Observatorievägen 90, Råö, 43992 Onsala, Sweden

⁶Max-Planck-Institute for Extraterrestrial Physics, Giesenbachstrasse 1, 86748 Garching, Germany

⁷Centro de Astrobiología (CSIC-INTA), Torrejón de Ardoz Madrid, Spain

Received 2024 October 23; revised 2025 June 30; accepted 2025 June 30; published 2025 September 4

Abstract

We present the results of astrochemical modeling of complex organic molecules (COMs) in the ice and gas of the prestellar core L1544 with the recently updated MONACO rate equation-based model. The model includes, in particular, nondiffusive processes, new laboratory verified chemical routes for acetaldehyde and methane ice formation, and variations of H and H₂ desorption energies depending on the surface coverage by H₂ molecules. For the first time, we simultaneously reproduce the abundances of several oxygen-bearing COMs in the gas-phase, the approximate location of the peak of methanol emission, as well as the abundance of methanol in the icy mantles of L1544. Radical–radical reactions on the grain surface between species such as CH₃, CH₃O, and HCO efficiently proceed nondiffusively. COMs are delivered to the gas-phase via chemical desorption amplified by the loops of H-addition/abstraction surface reactions. However, gas-phase chemical reactions as well provide a noticeable input to the formation of COMs in the gas, but not to the COMs solid-state abundances. This particularly applies for CH₃CHO and CH₃OCH₃. The simulated abundances of COMs in the ice are in the range 1%–2% (for methyl formate ice) or ~0.1% (for CH₃CHO and CH₃OCH₃) with respect to the abundance of H₂O ice. We stress a similarity between the simulated abundances of icy COMs in L1544 and the abundances of COMs in the gas-phase of hot cores/corinos. We compare our nondiffusive model with the diffusive model and provide constraints for the species' diffusion-to-desorption energy ratios.

Unified Astronomy Thesaurus concepts: [Astrochemistry \(75\)](#); [Interstellar dust processes \(838\)](#); [Interstellar abundances \(832\)](#); [Star formation \(1569\)](#); [Complex organic molecules \(2256\)](#); [Chemical reaction network models \(2237\)](#)

1. Introduction

In astrochemistry, complex organic molecules (COMs) are usually defined as carbon-bearing species containing six or more atoms (see, e.g., E. Herbst & E. F. van Dishoeck 2009). COMs are detected at all stages of star formation. Their detection in cold dark gas of the earliest stages of low-mass star formation was unexpected. Probably, the first detection of a nearly saturated COM toward a cold dark cloud was given by N. Marcelino et al. (2007), who reported the discovery of propylene, CH₂CHCH₃, toward TMC-1. The detection of O-bearing COMs in cold dense cores took place in 2012 (A. Bacmann et al. 2012; J. Cernicharo et al. 2012). During the last decade, COMs were found in many cold cores that appear to be on different stages of chemical and dynamical evolution along the star formation process, defined by central number densities, a density profile, and deuterium fraction (A. Crapsi et al. 2005; E. Keto & P. Caselli 2008). The most dynamically evolved starless cores, on the verge of star formation, are named prestellar cores. COMs were detected in L1521E (Z. Nagy et al. 2019; S. Scibelli et al. 2021), L1517B

(A. Megías et al. 2023), and L1498 (I. Jiménez-Serra et al. 2021), which can be considered starless cores, as well as in L1544 (I. Jiménez-Serra et al. 2016; P. Caselli et al. 2022), which is a prestellar core. An attempt to establish an evolutionary sequence of starless cores has been recently made by A. Megías et al. (2023). Different evolutionary statuses possibly explain observed differences in abundances of COMs across the cores. Thus, currently, it is possible to assert that COMs are ubiquitous at the earliest stages of the evolution of low-mass star-forming regions.

Although COMs have been detected toward many starless and prestellar cores, their distribution within the cores remains unknown, with the exception of methanol. In starless and prestellar cores, methanol is most abundant in a shell around the dust emission peak (e.g., M. Tafalla et al. 2002; L. Bizzocchi et al. 2014). This area is often referred to as methanol emission peak, or “methanol peak.” In turn, the dust emission peak, or “dust peak” corresponds to the part of the core with the highest gas density. According to the model by E. Keto & P. Caselli (2010), in L1544, the gas density at the dust peak exceeds 10⁷ cm⁻³ with A_V > 50, while the methanol peak is characterized by the moderate density of 10⁵ cm⁻³ and A_V ≈ 5. The two peaks are separated by ≈4000 au from each other (L. Bizzocchi et al. 2014). The observations by I. Jiménez-Serra et al. (2016) revealed presence of COMs



Original content from this work may be used under the terms of the [Creative Commons Attribution 4.0 licence](#). Any further distribution of this work must maintain attribution to the author(s) and the title of the work, journal citation and DOI.

toward both peaks in L1544 with abundances higher by a factor of ≈ 2 –10 toward the methanol peak than toward the dust peak.

During the last decade, several scenarios explaining the presence of COMs in cold dense molecular gas were proposed based on the possible role of cosmic rays, Eley-Rideal kinetics, and surface carbon insertion reactions (e.g., M. Ruaud et al. 2015; C. N. Shingledecker et al. 2018; J. B. Bergner et al. 2017). Essentially, the majority of proposed scenarios can be divided into two classes based on whether gas-phase chemistry or chemistry on interstellar grains is responsible for the formation of COMs. The first proposed scenario (A. I. Vasyunin & E. Herbst 2013) relied on gas-phase formation of COMs from precursors formed on grains (methanol). The model by A. I. Vasyunin & E. Herbst (2013) and its extended version (A. I. Vasyunin et al. 2017) were partially successful in explaining the observed abundances of COMs in L1689b and B1-b, as well as abundances and the spatial distribution of COMs in L1544. Nevertheless, the scenario faced several difficulties. First, methanol appeared to be overproduced in the gas-phase. Second, when applied to other starless cores that are presumably less evolved, the model failed to reproduce observed abundances of some COMs (e.g., S. Scibelli et al. 2021). Finally, the model by A. I. Vasyunin et al. (2017) was not able to produce appreciable amounts of CO_2 in the ice under the physical conditions of the static model of L1544 taken from E. Keto & P. Caselli (2010). In that model of L1544, the dust temperature is below 10 K in the inner part of the core and reaches about 15 K at its outer edge. According to K. I. Öberg et al. (2011) and A. C. A. Boogert et al. (2015), CO_2 is one of the major ice constituents with an abundance of more than 20% w.r.t. solid water, although it is not completely clear whether or not such high abundance holds in the inner parts of cold dense cores. Similar abundance ratios of CO_2 and water ices (10%–20%) are also found in dense molecular clouds according to the results of the Ice Age program (M. K. McClure et al. 2023; E. Dartois et al. 2024).

The model by A. I. Vasyunin & E. Herbst (2013) and A. I. Vasyunin et al. (2017) strongly relied on the parameterization of reactive desorption (RD) proposed in M. Minissale et al. (2016b). This parameterization is based on a pioneering series of experiments aimed at quantifying this important process (M. Minissale & F. Dulieu 2014; S. Cazaux et al. 2016). RD is a process of ejection of product(s) of an exothermic surface reaction to the gas-phase during the relaxation of energy released in the reaction event. The quantification of this process is difficult, as its efficiency depends on many factors including the properties of the underlying surface, binding energies, and complexity of product species, etc. The formula for the efficiency of RD (i.e., for the probability of product species of a reaction to desorb) proposed in M. Minissale et al. (2016b) predicts a wide range of efficiencies for products of various surface reactions, including large efficiencies (5% or more) in some cases. For example, H_2CO is likely overproduced in the gas-phase in A. I. Vasyunin et al. (2017) due to high RD efficiency of CH_3 and H_2CO itself. High abundances of gaseous O_2 and H_2O are related to the extremely high RD efficiencies ($>60\%$) for the surface reaction $\text{O} + \text{O} \rightarrow \text{O}_2$. Several other species such as H_2S have surface formation channels with high RD efficiencies ($>10\%$).

Later studies reported on average lower and more similar efficiencies for RD (K. J. Chuang et al. 2018; Y. Oba et al. 2018; K. Furuya et al. 2022; J. C. Santos et al. 2023). Estimated values of RD efficiency vary in the range of 1%–3% with significant uncertainties. Also, a new parameterization of RD was proposed in A. Fredon & H. M. Cuppen (2018) in addition to the earlier parameterizations by R. T. Garrod et al. (2007) and M. Minissale et al. (2016b). Thus, while extending our knowledge on RD and confirming that it is a ubiquitous phenomenon, the aforementioned studies also proved that quantitative estimation of RD efficiency still may contain significant uncertainties. Therefore, experimental data on RD should be taken with caution when including it into astrochemical models. As a result, it is reasonable to consider more conservative parameterizations of RD (e.g., R. T. Garrod et al. 2007).

While it was shown that, at least under certain assumptions, COMs in the cold gas can be formed in gas-phase chemical reactions, the role of chemistry on interstellar grains to synthesize COMs at ~ 10 K was assessed very differently in previous studies. While in some works (N. Balucani et al. 2015; D. Skouteris et al. 2018) this role was found secondary, newer studies suggest grain-surface chemistry plays a pivotal role in the detriment of gas-phase chemistry (M. Jin & R. T. Garrod 2020). The novel view on grain-surface chemistry as a key source of COMs at low temperatures (~ 10 K) is based on experimental findings by G. Fedoseev et al. (2015), T. Butscher et al. (2016), and S. Ioppolo et al. (2021). In those works, it was shown that COMs containing multiple carbon atoms, such as glycol aldehyde, ethylene glycol, and even the simplest amino acid, glycine, are efficiently formed in the laboratory experiments under physical conditions similar to those in cold dark clouds. Such results cannot be explained within the traditional paradigm of grain-surface chemistry that is based on the assumption that chemical reactions on grains proceed solely via the diffusive Langmuir–Hinshelwood mechanism. At 10 K, only the lightest species, which are atomic and molecular hydrogen, shall be sufficiently mobile on the surface to induce efficient diffusive chemical reactions; see T. I. Hasegawa et al. (1992). As a result, by means of diffusive chemistry at 10 K and below, only hydrogenation reactions can occur. Radical–radical reactions that are required to form COMs efficiently proceed on grains at $T \sim 30$ –40 K (R. T. Garrod & E. Herbst 2006), and are not efficient at 10 K because radicals are immobile at this temperature. Similarly, reactive atoms heavier than hydrogen shall be poorly mobile as well.

One of the possible ways to explain the results of G. Fedoseev et al. (2015) and S. Ioppolo et al. (2021) is to assume that radical–radical chemical reactions leading to the formation of complex organic species are still efficient at 10 K. This is due to statistical probability for the otherwise immobile radicals to appear next to each other as the products of processes that are efficient at 10 K. Such processes include accretion from the gas phase and production in efficient diffusive surface reactions, photo-induced reactions, and cosmic-ray-induced reactions. Thus, one can assume that chemical reactions on the surface between immobile species appearing next to each other can occur beyond the diffusive Langmuir–Hinshelwood mechanism, i.e., nondiffusively. As a result, COMs as well as other species such as CO_2 that cannot be formed at 10 K in the chemical models utilizing the

traditional diffusive paradigm can be produced via nondiffusive chemical reactions on the grain surface.

Basic mathematical formulation of nondiffusive surface chemistry suitable for inclusion into rate equation-based astrochemical models has been proposed by M. Jin & R. T. Garrod (2020). They studied the role of nondiffusive chemistry on the formation of COMs in the L1544 prestellar core (M. Jin & R. T. Garrod 2020), as well as the role of nondiffusive chemistry in the formation of icy mantles of interstellar grains in the Cha-MMS1 Class 0 protostar (M. Jin et al. 2022), and in the formation of COMs in hot cores (R. T. Garrod et al. 2022). The new models generally successfully reproduce the observed values of abundances of COMs in the gas-phase, and typical composition of interstellar ices. However, in the case of the prestellar core L1544, the model by M. Jin & R. T. Garrod (2020) has difficulty in reproducing the radial profiles of methanol and other complex organic species measured by I. Jiménez-Serra et al. (2016). Importantly, M. Jin & R. T. Garrod (2020) also conclude that gas-phase chemistry does not contribute significantly to the formation of COMs in L1544. This is in contrast to the earlier work by A. I. Vasyunin et al. (2017) who claimed that gas-phase chemical reactions play an important role in the formation of COMs toward the same prestellar core.

The goal of this study is to investigate the impact of nondiffusive chemical processes in icy mantles of interstellar grains on the formation of COMs in gas and ice under the conditions typical of the earliest stages of low-mass star formation. For that, we modify the MONACO code by adding the description of nondiffusive chemical processes to it. Then, we apply the updated code to the 1D static physical model of L1544. The physical model of L1544 is the same as the one utilized in our previous study of COM chemistry (A. I. Vasyunin et al. 2017). This choice enables us to compare new results to those in A. I. Vasyunin et al. (2017), and thus reconsider the roles of gas-phase and grain-surface chemical processes in the formation of COMs in prestellar cores. With this goal, we also updated the utilized chemical network with some most recent laboratory and theoretical results.

The paper is organized as follows. In Section 2, modifications introduced to the MONACO code and the physical model of L1544 are described. In Section 3, results are presented obtained with the model that includes enabled nondiffusive chemical processes and treatment of RD described in R. T. Garrod et al. (2007). Consequently, these results are compared with the results of the model with nondiffusive chemical processes but with RD treatment following M. Minissale et al. (2016b). In Section 4, the results of this study are discussed. Finally, in Section 5, the summary of this study is given.

2. Model

2.1. A Three-phase Code with Nondiffusive Chemistry

Our astrochemical model is based on the three-phase code MONACO described in A. I. Vasyunin et al. (2017), which treats the gas-phase, outer layers of icy mantles of interstellar grains, and the bulk ice as distinct phases interacting with each other. The code utilizes chemical rate equations to govern chemistry in each of the three phases. Several important updates are introduced to the original model. Those include treatment of nondiffusive chemistry on the ice surface and in

the icy bulk, dependence of H and H₂ binding energies on the H₂ surface coverage, and reaction/diffusion competition for barrier-mediated chemical reactions in the solid phase. As in similar models, gas-phase rate equations are given with the expression

$$\begin{aligned} \frac{dn_i^{\text{gas}}}{dt} = & \sum_{j,l} k_{jl}^{\text{gas}} n_j^{\text{gas}} n_l^{\text{gas}} - n_i^{\text{gas}} \sum_j k_{ij}^{\text{gas}} n_j^{\text{gas}} \\ & + \sum_j k_{\text{ext},j}^{\text{gas}} n_j^{\text{gas}} - k_{\text{ext},i}^{\text{gas}} n_i^{\text{gas}} \\ & - k_{\text{ads},i} n_i^{\text{gas}} + R_{\text{des},i}, \end{aligned} \quad (1)$$

where $n_{i(j,l)}^{\text{gas}}$ is the gas-phase abundance (per cubic centimeter) of the species $i(j, l)$, k_{ij} and k_{ji} are the rate coefficients for gas-phase two-particle reactions, $k_{\text{ext},i}$ and $k_{\text{ext},j}$ are the rate coefficients for the reactions caused by external factors (those reactions are cosmic-ray ionization, photoionization, cosmic-ray-induced photoreactions), $k_{\text{ads},i}$ is the adsorption rate coefficient for the i th species, and $R_{\text{des},i}$ is its desorption rate.

Desorption processes included in the model are thermal evaporation, cosmic-ray-induced desorption (T. I. Hasegawa & E. Herbst 1993), desorption by cosmic-ray-induced UV-photons (S. S. Prasad & S. P. Tarafdar 1983), photodesorption, and chemical (or reactive) desorption. The photodesorption yield per incident photon of 10^{-5} is assumed for all species except CO (M. Bertin et al. 2016; G. A. Cruz-Diaz et al. 2016). For carbon monoxide, a different yield equal to 10^{-2} is adopted (E. C. Fayolle et al. 2011). A more detailed discussion on the implication of photodesorption yields on modeling results can be found in A. Punanova et al. (2022).

Chemistry on the ice surface and within the ice bulk is governed by the following equations:

$$\frac{dn_i^{\text{sur}}}{dt} = \left(\frac{dn_i^{\text{sur}}}{dt} \right)^{\text{chem}} - \left(\frac{dn_i^{\text{sur}}}{dt} \right)^{\text{tran}} - R_i^{\text{diff,s2b}}, \quad (2)$$

$$\frac{dn_i^{\text{bulk}}}{dt} = \left(\frac{dn_i^{\text{bulk}}}{dt} \right)^{\text{chem}} + \left(\frac{dn_i^{\text{sur}}}{dt} \right)^{\text{tran}} - R_i^{\text{diff,b2s}}. \quad (3)$$

Here, n_i^{sur} is the abundance of i th species on the surface, and n_i^{bulk} is the abundance of i th species in the bulk. The first term in the right side of Equation (2) describes the evolution of the abundance of species i due to chemical reactions on the surface, accretion, and desorption. In Equation (3), the first term includes chemical reactions in the bulk ice. The second and third terms in Equations (2) and (3) describe the transport of chemical species between the surface layers of icy mantles and the bulk ice. They are explained below.

In this work, we consider both diffusive and nondiffusive chemical reactions on the grain/ice surface. The diffusive mechanism of surface reactions implies that a reaction occurs when two reactants encounter each other on the surface as a result of a 2D random walk. In other words, at least one reactant must be mobile on the surface under the physical conditions of interest. At grain temperatures below 10 K, typical of prestellar cores, only atomic and molecular hydrogen are believed to be highly mobile due to their low binding energies to the surface or, possibly, due to quantum tunneling through the potential barriers between binding sites on the surface. However, it is also possible that two reactants appear on the surface in close proximity to each other, already

in a position to react. The reactants may appear as products of a prior chemical reaction, or accrete from the gas. In this case, the mobility of reactants is not necessary for a reaction to occur, and reactions between heavier species such as radicals can proceed at low temperatures.

Diffusive chemical reactions in the first term of Equations (2) and (3) can be described similarly as gas-phase reactions in Equation (1) or using the modified rate equations approach (R. T. Garrod 2008; R. T. Garrod et al. 2009). Nondiffusive chemical reactions on the surface and in the bulk are introduced following the approach by M. Jin & R. T. Garrod (2020). The expression for the rate of a nondiffusive chemical reaction is as follows:

$$R_{AB} = f_{\text{act}}(AB)R_{\text{comp}}(A)\frac{N_B}{N_S} + f_{\text{act}}(AB)R_{\text{comp}}(B)\frac{N_A}{N_S}, \quad (4)$$

where $f_{\text{act}}(AB)$ is a reaction efficiency for barrier-mediated reactions calculated taking into account reaction-diffusion competition (see below), N_A and N_B are the average numbers of atoms or molecules of the reactants on a single grain, N_S is the binding sites number on the surface of an average grain, and $R_{\text{comp}}(i)$ is the so-called “completion rate” for the i th species. In the case of the regular diffusive mechanism, the “completion rate” would be equal to $k_{\text{hop}}(i)N_i$. This would account for the events of the appearance of the reactant i as the result of hopping. In the case of the nondiffusive mechanism implementation, the completion rate is equal to

$$R_{\text{comp}}(A, B) = \frac{1}{1/R_{\text{app}}(A, B) + t_{AB}}. \quad (5)$$

Here, $R_{\text{app}}(A, B)$ is an “appearance rate” for species A or B , i.e., the sum of rates of all processes that “deliver” reactants A or B on the surface (M. Jin & R. T. Garrod 2020). Those processes could be accretion from the gas-phase, photoreactions in the ice, surface diffusive reactions, etc. The t_{AB} is a timescale against any possible event to occur to species A and B when they are already in a position to react.

To the MONACO code, we introduced all types of nondiffusive chemical processes described in M. Jin & R. T. Garrod (2020) except “three-body excited reactions.” Also, in this study, we prefer to name “three-body reactions” as “sequential reactions,” as, in chemistry, termolecular reactions are often referred to as “three-body,” and because, in our point of view, the term “sequential” better reflects the essence of occurring nondiffusive reactivity. The individual impact of all considered nondiffusive mechanisms is discussed in Section 4.

M. Jin & R. T. Garrod (2020) allow three rounds of nondiffusive sequential reactions. They note that the impact of nondiffusive processes on species’ abundances diminishes after the second round. In our simulations, the influence of nondiffusive reactions is negligible after the third round; thus, we have also chosen to perform three rounds.

The reaction efficiency $f_{\text{act}}(AB)$ for reactions with activation barriers is calculated taking into account so-called “reaction-diffusion competition.” The existence of an activation barrier effectively means that, at any single encounter of reactants, the probability of a reaction event to occur is below unity. When two reactants of a barrier-mediated surface reaction stay next

to each other, two possibilities compete: the possibility to react and the possibility to “diffuse away” from each other. The resulting probability of a reaction between species A and B to occur thus is

$$f_{\text{act}}(AB) = \frac{\nu_{AB}\kappa_{AB}}{\nu_{AB}\kappa_{AB} + k_{\text{hop}}(A) + k_{\text{hop}}(B)}, \quad (6)$$

where ν_{AB} is the highest of the vibrational frequencies of reactants A and B , κ_{AB} is the probability for the reaction to occur, and $k_{\text{hop}}(A)$ and $k_{\text{hop}}(B)$ are the thermal hopping rates for species A and B , correspondingly (T. I. Hasegawa et al. 1992).

The second term in Equations (2) and (3) is responsible for redefining the surface when existing surface material is “buried” to the bulk by newly accreted species, or, on the contrary, “excavated” from the bulk when surface material is desorbed, or its amount is changed due to surface chemical reactions. Expressions (4) and (5) in A. I. Vasyunin et al. (2017) describe the second term completely. Note that the parameter α_{tran} in their Expression (4) is defined as in R. T. Garrod & T. Pauly (2011). The third term in Equations (2) and (3) describes thermal diffusion of material between the surface layers and the bulk ice. We utilized the basic expression for bulk-surface diffusion given in R. T. Garrod (2013), although a more elaborated approach exists (R. T. Garrod et al. 2017). However, at the very least, for low dust temperatures typical of prestellar cores, the rates of such diffusion shall be slow and will not affect modeling results significantly.

In contrast to A. I. Vasyunin et al. (2017), in the current model, we allow H_2 accretion on grains. Indeed, this is the most abundant molecule in molecular clouds with the abundance 10^4 times higher than the undepleted abundance of the second most abundant gas-phase molecule, carbon monoxide (CO). This ensures the huge accretion rate of H_2 . Since the dust temperature in dark regions of prestellar cores is likely to be lower than 10 K (see, e.g., A. Crapsi et al. 2007), one may expect the significant abundance of H_2 on grain surfaces despite the low binding energy of this species. Moreover, the simulations may lead to a nonphysical result of an almost complete freeze-out of H_2 from the gas-phase, and the building up of giant icy mantles that consist mainly of solid H_2 .

To avoid a nonphysical scenario of the complete freeze-out of H_2 at low temperatures, in our new model, binding energies of H and H_2 are adjusted according to the surface composition—namely, to the surface fraction covered by H_2 , following the approach proposed in R. T. Garrod & T. Pauly (2011). Following H. M. Cuppen et al. (2009), they note that binding on the mixed surface composed of H_2 and H_2O is weaker than on that composed of pure H_2O ice. Since H. M. Cuppen et al. (2009) also estimated the binding energy to H_2 surface as about 10 times weaker than to CO surface, R. T. Garrod & T. Pauly (2011) suggested an expression for the time-dependent “effective desorption energy,”

$$E_{\text{des,eff}} = E_{\text{des}}(1 - \theta(\text{H}_2)) + 0.1E_{\text{des}}\theta(\text{H}_2). \quad (7)$$

Here, $\theta(\text{H}_2)$ is the fraction of the grain surface covered by molecular hydrogen. Therefore, the binding energy of a species becomes in general a time-dependent value. In R. T. Garrod & T. Pauly (2011), binding energies of all surface species are corrected using the expression in Equation (7). However, in our model, we apply it only for atomic and molecular hydrogen. The correction is not applied

to heavier species because it is possible that they can penetrate the surface H_2 layer and bind to heavier species below it (see G. W. Fuchs et al. 2009).

Diffusive chemistry in the bulk ice is also treated similarly as in A. I. Vasyunin et al. (2017) with the exception for chemical reactions with atomic and molecular hydrogen. In A. I. Vasyunin et al. (2017), following R. T. Garrod (2013), it was assumed that all diffusive chemical reactions that occur on the grain surface also proceed in the bulk ice via the swapping of species. The rate of swapping was calculated similarly to the rate of thermal diffusion but assuming that swapping energies E_{swap} of species in the bulk are twice as high as their surface diffusion energies E_{diff} . This reflects the assumption that binding energies of species in the bulk are twice higher than for the surface species because bulk species on average have twice as many neighbors. We made an exception for atomic and molecular hydrogen: it is assumed that swapping energies of H and H_2 in the bulk are only a factor of 1.5 higher than their surface diffusion energies. Atoms and molecules of hydrogen are geometrically smaller than other species in the ice. This may result in higher mobility of H and H_2 in the ice bulk in comparison to other species. In the models presented in this work, the bulk mobility of species other than H and H_2 has a limited impact on the chemical evolution of ice and gas.

The probability for H atoms to stick to the grain surface upon collision is calculated according to D. Hollenbach & C. F. McKee (1979) and depends on the dust temperature. The sticking probabilities for other species are taken as unity (see, e.g., A. P. Jones & D. A. Williams 1985). Other suggested values and the impact of the sticking probabilities on the modeling results are discussed in Section 4.4.

Chemical processes on the ice surface and in the bulk ice induced by cosmic rays and UV-photons are treated as in the gas-phase. Cross sections of photoprocesses on the surface are equal to that of the corresponding processes in the gas-phase. Note that photodissociation rates in the ice can be smaller than corresponding rates in the gas-phase (see, e.g., K. I. Oberg 2016; D. M. Paardekooper et al. 2016; J. Kalvans 2018). Radiolysis of interstellar ices and their laboratory analogs has been studied extensively in recent years (S. Pilling et al. 2010; G. Fedoseev et al. 2018; C. N. Shingledecker et al. 2018, 2019, 2020; A. V. Ivlev et al. 2023). The results of those works suggest that the impact of cosmic rays on the chemistry of interstellar ices is more complicated than it is assumed in our model. On the other hand, G. Fedoseev et al. (2018) investigated the formation of OCN^- by cosmic-ray processing of N_2 - and NH_3 -containing interstellar ice analogs. The results suggest that in dense dark clouds significant processing of N_2 -containing ices by cosmic rays requires timescales of $\sim 10^6$ – 10^7 yr. At the same time, dynamical and chemical timescales of evolution in prestellar cores are approximately 1–2 orders of magnitude shorter. Thus, we believe that the aforementioned simplistic approach to cosmic-ray processing of ices “as in the gas-phase” is sufficient for this work.

2.2. Physical Model of L1544 and Initial Conditions for Chemistry

The physical model of L1544 prestellar core and initial conditions for chemistry are similar to those used in A. I. Vasyunin et al. (2017). In particular, we use a static 1D radial profile of gas density, dust, and gas temperatures in L1544 with central densities of $\sim 10^7 \text{ cm}^{-3}$ first obtained in

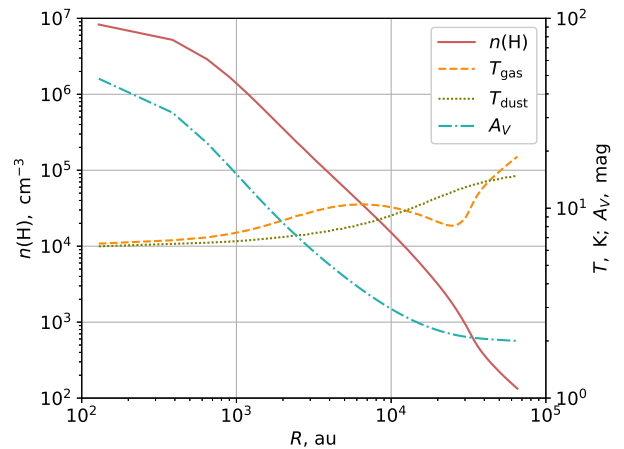


Figure 1. The radial profile of physical conditions in L1544 from E. Keto & P. Caselli (2010). The dust temperature in the interior of the core is below 10 K.

E. Keto & P. Caselli (2010) and confirmed recently by P. Caselli et al. (2019, 2022; see Figure 1). The visual extinction at the edge of the core in our modeling equals 2 mag to simulate the fact that L1544 is embedded in a molecular cloud (E. Redaelli et al. 2022). There are 128 radial points in our profile. In every point, chemical evolution is calculated independently with our 0D MONACO model. Initial abundances for the calculation of the prestellar core chemistry are the same in every radial point and taken as the final chemical composition of a “translucent cloud” after 10^6 yr of evolution. The “translucent cloud” is characterized by a gas density of 10^3 cm^{-3} and visual extinction $A_V = 2.0$ mag. During the 10^6 yr of evolution, gas and dust temperatures linearly drop from 15 to 10 K. The initial abundances for the translucent cloud phase are atomic “low metals” values listed in Table 1 in V. Wakelam & E. Herbst (2008). Hydrogen is assumed to initially reside in a molecular form.

Grain-surface chemistry in cold dark environments is mainly controlled by the mobility of species. In classic gas-grain astrochemical models, only diffusive grain-surface chemistry is considered (e.g., T. I. Hasegawa et al. 1992), so the diffusion rates of species are the natural control parameters. In the new grain-chemistry models that include nondiffusive chemical processes, the diffusion rates may seem to be less crucial. However, they still are, as diffusion rates render the relative importance of diffusive and nondiffusive chemical reactions that occur simultaneously. In this work, we assume that all species diffuse on the surface and in the bulk only via thermal hopping. There is still a debate on whether quantum tunneling plays an important role in the diffusion of atomic and molecular hydrogen at low temperatures (e.g., N. Watanabe et al. 2010; T. Hama et al. 2012; T. Hama & N. Watanabe 2013; H. M. Cuppen et al. 2017). However, it is likely that the diffusion of H atoms on amorphous water ice is much slower than predicted by the simple model of tunneling through rectangular potential barriers (T. I. Hasegawa et al. 1992) even if quantum tunneling through diffusion barriers indeed contributes to its rate along with thermal hopping (K. Kuwahata et al. 2015; B. Senevirathne et al. 2017). Thus, we assume only thermal hopping for H and H_2 mobility. The quantum tunneling through reaction activation barriers is enabled, and the barriers are assumed to be rectangular with the width of 1 Å. Several reactions included in the CO

Table 1
Summary of Parameters of Considered Chemical Models

Parameter	Value
Cosmic-ray ionization rate (s^{-1})	1.3(-17)
Photodesorption yield for CO (mol/photon)	1.0(-2) ^a
Photodes. yield, other species (mol/photon)	1.0(-5) ^{b,c}
Grain size (cm)	1.0(-5)
Dust-to-gas mass ratio	1.0(-2)
Surface site density (cm^{-2})	1.5(+15)
Grain density ($g\ cm^{-3}$)	3.0
E_{diff}/E_{des} , atomic species	0.5
E_{diff}/E_{des} , # atoms > 1	0.3
E_{swap}/E_{diff} , H and H ₂	1.5
E_{swap}/E_{diff} , other species	2.0
Number of “surface” monolayers	4 ^d
Number of rounds for nondiffusive reactions	3 ^e
Tunneling through diffusion barriers	Off ^e
Hopping/reaction activation competition	On ^f
Tunneling through reaction barriers	On
Reaction bar. width, Å (exceptions: see Table 7)	1.0

Notes.

^a E. C. Fayolle et al. (2011).

^b M. Bertin et al. (2016).

^c G. A. Cruz-Díaz et al. (2016).

^d A. I. Vasyunin & E. Herbst (2013).

^e M. Jin & R. T. Garrod (2020).

^f R. T. Garrod & T. Pauly (2011); $x(y)$ means $x \times 10^y$.

hydrogenation chain have different barrier widths (see Appendix B).

Rates of thermal hopping in rate equation-based models are typically controlled by the diffusion-to-desorption energy ratio (s), E_{diff}/E_{des} . In principle, there is no fundamental physical argument that E_{diff}/E_{des} shall be the same for all species on the surface (A. Fredon et al. 2021). Taking this into account, and the results of M. Minissale et al. (2016a) and L. J. Karssemeijer & H. M. Cuppen (2014), we adopted $E_{diff}/E_{des} = 0.5$ for atomic species and $E_{diff}/E_{des} = 0.3$ for molecular species. Note that K. Furuya et al. (2022) reported a wide range of diffusion-to-desorption energy ratios (0.2–0.7) depending on species. In Section 4.3, we discuss how the change in these parameters modifies the results of the simulations.

In this work, we compare two models with different parameterizations of RD. The first is based on Rice–Ramsperger–Kessel theory and introduced in an astrochemical context by R. Garrod et al. (2006) and R. T. Garrod et al. (2007; hereafter, GRD model). The value of the parameter a in Expression (2) in R. T. Garrod et al. (2007) for the probability of RD is taken equal to 0.01. The second parameterization of RD considered in this study is based on experimental findings by M. Minissale et al. (2016a; hereafter MRD). It was utilized in the study by A. I. Vasyunin et al. (2017) and was recently updated in W. Riedel et al. (2023). In this work, we utilize it with the previously used value of the effective mass of the surface element M equal to 100 a.m.u. Note that, even where the treatment of RD efficiency follows R. T. Garrod et al. (2007), it is allowed only from the nonwater fraction of the ice surface, as discussed in A. I. Vasyunin et al. (2017). The key parameters of the utilized models are summarized in Table 1. The major updates to the chemical network are described in Appendix B.

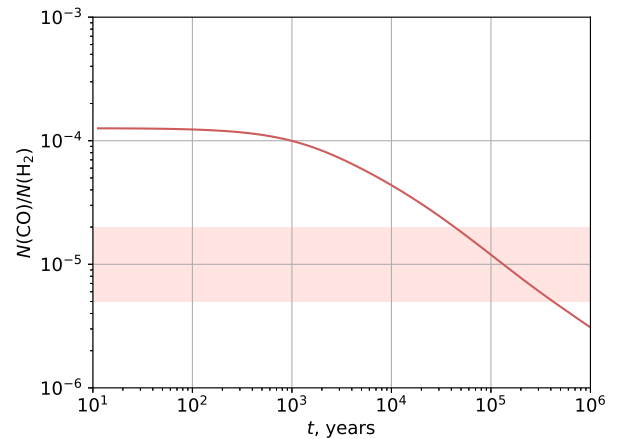


Figure 2. Temporal evolution of gas-phase CO-to-H₂ column density ratio in our simulations. Colored area denotes the factor of 2 uncertainty for the observed CO depletion factor taken from P. Caselli et al. (1999).

3. Results

3.1. CO Depletion Factor in Models

A comparison of modeling results with the observational data requires the establishment of some formal approach. Below, we describe the approach utilized in this work. First, it is applied to the comparison of the results of the GRD model with the observed abundances of COMs in L1544. Then, in Section 3.5, it is utilized to test the results of the MRD model against the same observations.

As in A. I. Vasyunin et al. (2017), to determine the range of evolutionary time where modeled and observed abundances can be compared, we calculated the temporal evolution of CO depletion factor toward the dust continuum peak (which is considered to be the core center) in the model, and compared it to the observed value obtained by P. Caselli et al. (1999). According to their data, CO experiences significant depletion in the central parts of the prestellar core L1544—they estimate the observed CO depletion factor as ≈ 10 at the position of the dust peak. In Figure 2, the temporal evolution of CO-to-H₂ column density ratio in our GRD model is presented; from here on, every gas column density is convoluted with a Gaussian function representing the IRAM radio telescope beam with $FWHM = 26''$ (which is the beam size in the I. Jiménez-Serra et al. 2016 observations). The colored area denotes the factor of 2 uncertainty for the observed depletion factor of CO. In our modeling, the observed CO depletion factor is reached at $\approx 1.2 \times 10^5$ yr of the simulation time. However, the uncertainty margin of CO depletion covers the time range starting at $\approx 4.0 \times 10^4$ yr and up to $\approx 4.0 \times 10^5$ yr.

3.2. Definition for the Agreement of Modeling and Observational Results

In our spherical model of the physical structure of L1544, the dust peak is located in the center of the core, and the location of the methanol peak corresponds to the radial distance of 4000 au from the core center. Modeling results are compared to the observed values of abundances of species toward the dust peak and methanol peak reported in I. Jiménez-Serra et al. (2016).

To compare our modeling results with the observations, we created agreement maps in the phase space (t, R) , where t is a time moment in simulations, and R is a radial point in a

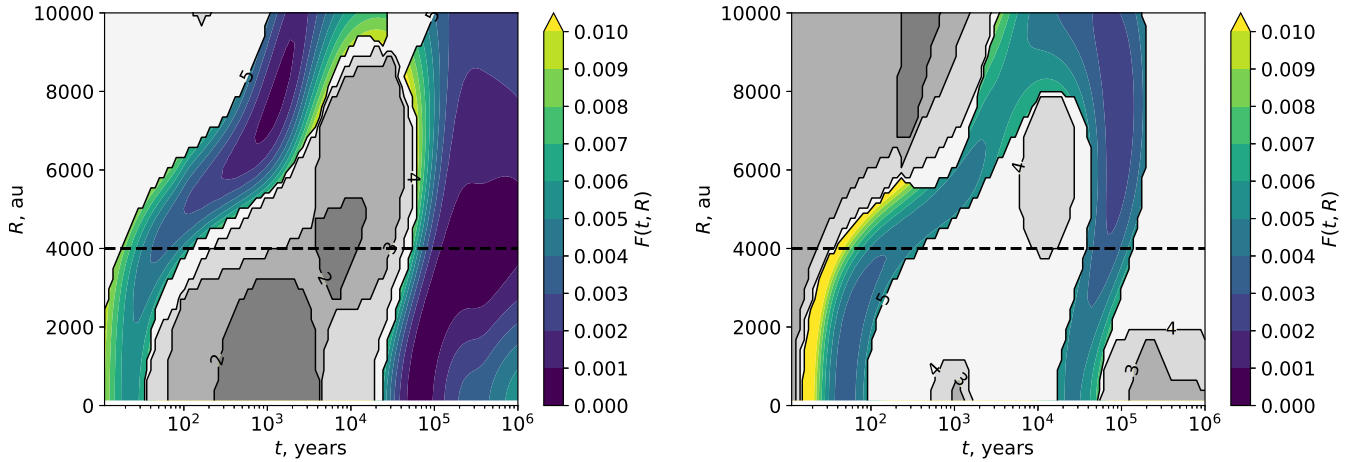


Figure 3. Agreement maps for the dust peak (left) and for the methanol peak (right) for the GRD model. Vertical axis represents the radial distance from the core center. Horizontal axis represents the evolutionary time in the model. The position of the dust peak corresponds to 0 au on vertical axis; the position of the methanol peak corresponds to 4000 au and is marked with a dashed horizontal line. Gray scale is for the areas where the abundances of ≤ 5 of studied species (CH_3OH , CH_3O , CH_3CHO , HCOOCH_3 , CH_3OCH_3 , NH_2CHO) are simultaneously in agreement with the observational data; numbers indicate the number of species that are simultaneously in agreement with the observations inside a contour line. The area with all the studied species are simultaneously in agreement with the observations is colored. The higher the $F(t, R)$ value defined in Equation (8), the worse the agreement with the observations; 0.000 means complete agreement. (We do not show similar agreement maps for the MRD model since there is no (R, t) domain for which simultaneous agreement for all the studied species is attained.)

spherically symmetric model of L1544. In the left panel of Figure 3, we show a comparison of the abundances obtained by our model with the abundances observed toward the dust peak in L1544, while, in the right panel, we present a comparison of modeled abundances to the abundances observed toward the low-density, CH_3OH -rich shell detected by L. Bizzocchi et al. (2014) at ≈ 4000 au from the continuum peak (the “methanol peak”). For the comparison, we use the gas species CH_3OH , CH_3O , CH_3CHO , HCOOCH_3 , CH_3OCH_3 , and NH_2CHO . We are primarily interested in those phase areas where the modeled abundances of all the species used for the comparison are *in agreement* with observed values. By *agreement*, we mean the situation when the modeled abundance at a certain moment of time differs no more than by an order of magnitude from the observed value. If an upper limit is established for a species from observations, we consider its modeled abundance to be *in agreement* with an upper limit if the modeled abundance is less than or exceeds by no more than an order of magnitude the observed upper limit. Upper limit means nondetection of a species, and exceeding the limit by more than an order of magnitude may be astrochemically interpreted as a poor agreement with observations. Those areas of the parameter space where the modeled abundances of all six species are *in agreement* with observations are filled with color. The areas where five or fewer species have abundances *in agreement* with the observational results are filled with gray scale (the darker the filling, the fewer species have abundances *in agreement* with the observational values). The colors inside the best-fit area denote the values of the function $F(t, R)$, which resembles the function in Equation (17) from A. I. Vasyunin et al. (2017):

$$F(t, R) = \sum_{i=1}^6 \left(\frac{\log \chi_{\text{obs}}(X_i) - \log \chi_{\text{mod}}^{(t,R)}(X_i)}{\log \chi_{\text{obs}}(X_i) + \log \chi_{\text{mod}}^{(t,R)}(X_i)} \right)^2, \quad (8)$$

where $\chi_{\text{obs}}(X_i)$ is the observed abundance of the species X_i (at the dust peak or at the methanol peak, correspondingly), and $\chi_{\text{mod}}^{(t,R)}(X_i)$ is the modeled abundance of the species X_i at the point (t, R) derived from the column densities. The modeled

abundances, in turn, are defined as $\chi_{\text{mod}}^{(t,R)}(X_i) = N_{\text{mod}}^{(t,R)}(X_i) / N_{\text{mod}}^{(t,R)}(\text{H}_2)$; here, $N_{\text{mod}}^{(t,R)}(X_i)$ is the modeled column density of the species X_i convoluted over the $26''$ Gaussian beam, and $N_{\text{mod}}^{(t,R)}(\text{H}_2)$ is the H_2 smoothed column density.

In the map for the dust peak (left panel of Figure 3), the minimum value of the function $F(t, R)$ —which indicates the best agreement with the observations—is reached at the distance of 3700 au from the core center at 3.9×10^5 yr of the simulation time for the GRD model. This time point is located on the border of the time interval allowed by the CO depletion factor. The lowest value of $F(t, R)$ for the methanol peak is reached at 7600 au and 10^5 yr of the simulation time, which fits the CO depletion timescale much better (see Figure 2). At 10^5 yr, all the species also demonstrate modeling abundances *in agreement* with the observed values both at the dust peak and at the observational methanol peak positions. Thus, in our modeling, we consider 10^5 yr as the time of the best agreement with the observational data. Note that our best agreement time is similar to the best-fit time from A. I. Vasyunin et al. (2017), which is equal to 1.6×10^5 yr.

3.3. Results of the GRD Model

Let us now consider modeling results in detail. Figure 4 presents the modeled fractional abundances of the studied gaseous species (top left) and the abundances derived as the ratios of the smoothed modeled column densities (top right) for the time of the best agreement with the observational data (10^5 years). Additionally, in Figure 10 (Appendix A) temporal evolution of abundances of gaseous species is presented. In Table 2, modeled abundances for the time of the best agreement are compared to the observed values. In contrast to A. I. Vasyunin et al. (2017), our model does not overproduce methanol. At the methanol peak, the model of A. I. Vasyunin et al. (2017) gives the $\chi(\text{CH}_3\text{OH})$ of 2.7×10^{-8} , while our model gives 1.2×10^{-9} , which is closer to 3.9×10^{-9} reported by A. Chacón-Tanarro et al. (2019) based on the IRAM 30 m single-dish observations. It should be noted that $\chi(\text{CH}_3\text{OH}) = 8.0 \times 10^{-9}$ used in

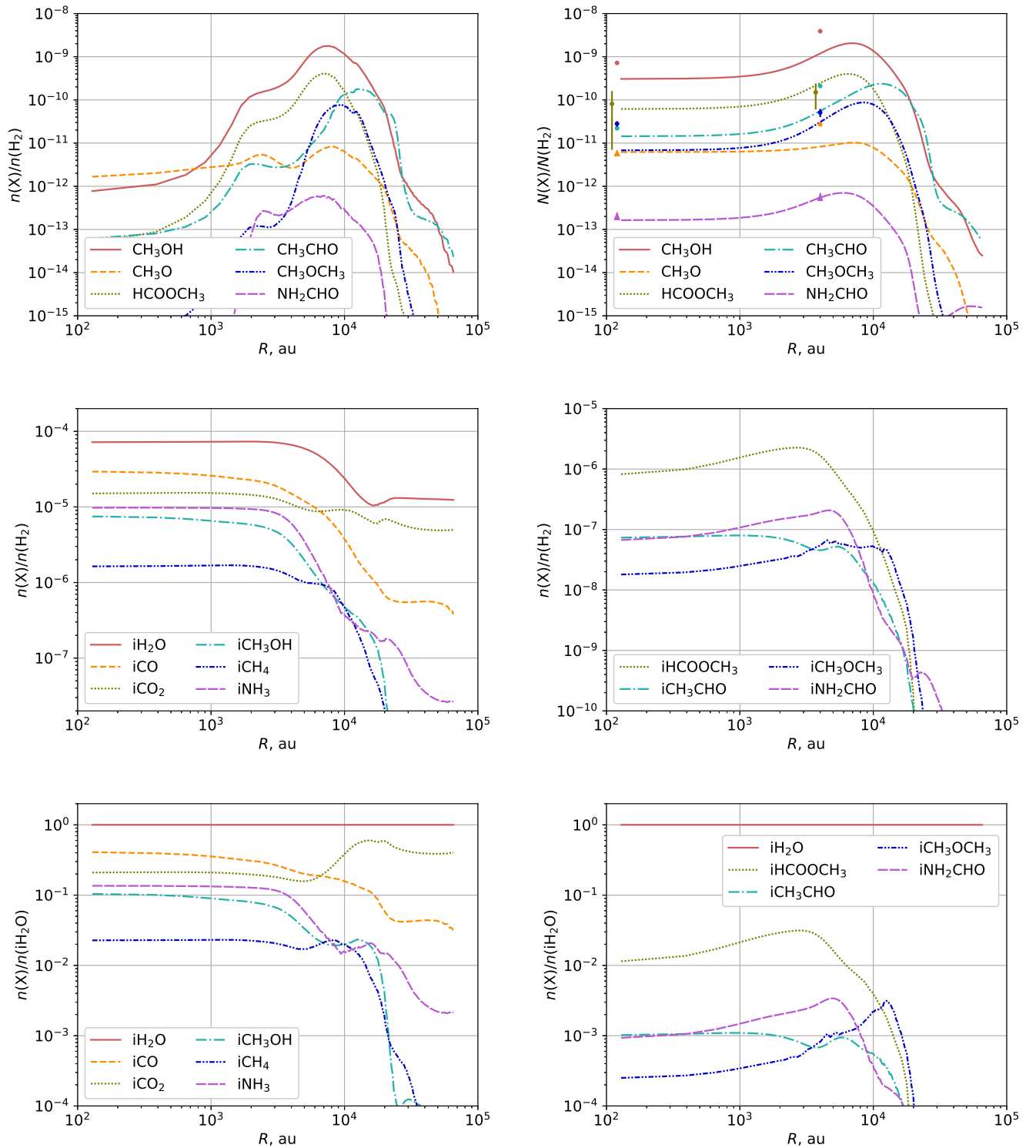


Figure 4. Radial profiles obtained with the model GRD at the time of the best fit with observational results (10^5 yr). Top: profiles of modeled abundances (top left) and abundances derived as column density ratios (top right) of complex organic species. Abundances derived as column densities are smoothed over the $26''$ Gaussian beam. Middle: profiles of abundances of major ice constituents (middle left) and selected complex organic molecules in the ice (middle right) w.r.t. H_2 . Bottom: same as in the middle, but w.r.t. solid H_2O . Colored dots in the top right panel denote observational values by A. Chacón-Tanarro et al. (2019) for CH_3OH and by I. Jiménez-Serra et al. (2016) for other species, vertical lines are for error bars, and arrows are for observational upper limits.

I. Jiménez-Serra et al. (2021) was obtained with a $\approx 5''$ beam of NOEMA (A. Puanova et al. 2018). Thus, such results should not be directly compared with the COM abundances obtained with the $26''$ beam.

The COMs-to-methanol gas-phase abundance ratios are significantly higher in the present model in comparison to

those in A. I. Vasyunin et al. (2017). At 4000 au, the modeled abundances of such COMs as CH_3OCH_3 , CH_3CHO , and HCOOCH_3 are 3%, 4%, and 21% of the modeled methanol abundance, correspondingly (see Table 3). In A. I. Vasyunin et al. (2017), the gap between modeled abundances of COMs and methanol abundance is generally wider: HCOOCH_3 and

Table 2

Observed Abundances of COMs in the Gas-phase $\chi_{\text{obs}}(X) = N_{\text{obs}}(X)/N_{\text{obs}}(\text{H}_2)$ in Comparison to Modeled Abundances of COMs

$\chi_{\text{mod}}(X) = N_{\text{mod}}(X)/N_{\text{mod}}(\text{H}_2)$ Derived from Smoothed Column Densities

Species	$\chi_{\text{obs}}(X)$ (cm^{-3})	$\chi_{\text{mod}}(X)$ (cm^{-3})
Dust Peak		
CH ₃ OH	$(7.2 \pm 0.8) \times 10^{-10}$	3.1×10^{-10}
CH ₃ O	$\leq(5.1 - 6.7) \times 10^{-12}$	6.2×10^{-12}
CH ₃ CHO	2.2×10^{-11}	1.3×10^{-11}
CH ₃ OCH ₃	$(2.8 \pm 0.4) \times 10^{-11}$	6.8×10^{-12}
HCOOCH ₃	$(8.1 \pm 7.4) \times 10^{-11}$	6.2×10^{-11}
NH ₂ CHO	$\leq(2.4 - 3.1) \times 10^{-13}$	1.6×10^{-13}
CH ₃ OH Peak		
CH ₃ OH	$(3.9 \pm 0.4) \times 10^{-9}$	1.2×10^{-9}
CH ₃ O	2.7×10^{-11}	8.3×10^{-12}
CH ₃ CHO	2.1×10^{-10}	5.0×10^{-11}
CH ₃ OCH ₃	$(5.1 \pm 1.1) \times 10^{-11}$	3.1×10^{-11}
HCOOCH ₃	$(1.5 \pm 0.9) \times 10^{-10}$	2.5×10^{-10}
NH ₂ CHO	$\leq(6.7 - 8.7) \times 10^{-13}$	5.4×10^{-13}

Note. $N_{\text{obs}}(X)$ for CH₃OH are obtained from A. Chacón-Tanarro et al. (2019); $N_{\text{obs}}(X)$ for the rest of species and $N_{\text{obs}}(\text{H}_2)$ toward the dust peak ($5.4 \times 10^{22} \text{ cm}^{-2}$) and the methanol peak ($1.5 \times 10^{22} \text{ cm}^{-2}$) are taken from I. Jiménez-Serra et al. (2016).

Table 3

Observed and Modeled Abundance Ratios $\chi(X)/\chi(\text{CH}_3\text{OH})$ of Selected COMs to CH₃OH in Percentages

Species	Dust Peak		CH ₃ OH Peak	
	Observ.	Model.	Observ.	Model.
CH ₃ CHO	3.1 ± 0.3	4.2	5.4 ± 0.6	4.2
CH ₃ OCH ₃	3.9 ± 0.6	2.2	1.3 ± 0.3	2.6
HCOOCH ₃	11.3 ± 10.3	20.0	3.8 ± 2.4	20.8

Note. The observational abundances for CH₃OH are taken from A. Chacón-Tanarro et al. (2019); the observational abundances for the rest of species are from I. Jiménez-Serra et al. (2016).

CH₃OCH₃ amount to 0.2% and 0.1% of the modeled methanol abundance, correspondingly, and CH₃CHO amounts to 2% of CH₃OH abundance. S. Scibelli et al. (2021) report the COMs-to-methanol ratios in prestellar cores derived from observations to be in a range from a few and up to $\approx 10\%$ (see their Figure 12). Our new model fits this range better than the previous one. The modeled radial distances of COMs peak abundances from the core center vary with species. While in the model the HCOOCH₃ and NH₂CHO peaks coincide with the methanol peak, peaks of CH₃CHO and CH₃OCH₃ are somewhat shifted from the methanol center. Such behavior is related to the formation routes of COMs. Some of the routes are not directly related to methanol (see below).

The composition of icy mantles of interstellar grains for the prestellar core L1544 in the current model differs from that in the model by A. I. Vasyunin et al. (2017), and may be considered as more reasonable. In Figure 4, the modeled fractional abundances $n(X)/n(\text{H}_2)$ of key ice components (middle left panel) and of ice COMs (middle right panel) are presented, as well as their fractional abundances w.r.t. the abundance of the water ice (bottom panels). Table 4 summarizes the ice fractional

Table 4

Modeled Abundances of the Most Important Ice Components and Ice COMs in L1544 ($n(X)$), Their Ratios to Ice H₂O Abundance in Percentage ($n(X)/n(\text{H}_2\text{O})$ in Percentages), and Calculated Column Densities $N(X)$

Species	$n(X)$ (cm^{-3})	$n(X)/n(\text{H}_2\text{O})$ (%)	$N(X)$ (cm^{-2})
Dust Peak			
iH ₂ O	7.2×10^{-5}	100.00	1.2×10^{19}
iCO	2.9×10^{-5}	40.86	4.5×10^{18}
iCO ₂	1.5×10^{-5}	21.07	2.5×10^{18}
iCH ₄	1.6×10^{-6}	2.27	2.7×10^{17}
iNH ₃	9.6×10^{-6}	13.44	1.6×10^{18}
iCH ₃ OH	7.5×10^{-6}	10.43	1.1×10^{18}
iCH ₃ CHO	7.3×10^{-8}	0.10	1.2×10^{16}
iCH ₃ OCH ₃	1.8×10^{-8}	0.02	4.0×10^{15}
iHCOOCH ₃	8.3×10^{-7}	1.15	2.0×10^{17}
iNH ₂ CHO	6.6×10^{-8}	0.09	1.5×10^{16}
CH ₃ OH Peak			
iH ₂ O	6.6×10^{-5}	100.00	7.5×10^{17}
iCO	1.5×10^{-5}	22.66	1.5×10^{17}
iCO ₂	1.1×10^{-5}	16.51	1.5×10^{17}
iCH ₄	1.2×10^{-6}	1.81	1.3×10^{16}
iNH ₃	5.9×10^{-6}	8.99	4.5×10^{16}
iCH ₃ OH	3.3×10^{-6}	4.95	2.7×10^{16}
iCH ₃ CHO	4.5×10^{-8}	0.07	5.4×10^{14}
iCH ₃ OCH ₃	5.4×10^{-8}	0.08	8.0×10^{14}
iHCOOCH ₃	1.7×10^{-6}	2.53	1.3×10^{16}
iNH ₂ CHO	1.9×10^{-7}	0.29	2.0×10^{15}

Notes. Ratios of column densities are not the same as ratios of abundances since column densities are integrated along the line of sight while the abundances belong to a certain spatial position in the core.

The prefix “i” denotes the total amount of a species in icy grain mantles, which is the sum of surface and bulk ice abundances. The calculated H₂ column density is 8.5×10^{22} for the dust peak and 7.9×10^{21} for the methanol peak.

abundances of selected species, their percentage to the H₂O ice abundance, and calculated column densities $N(X)$. Here and below, the prefix “g” denotes species in the surface layers of icy mantles. The prefix “b” denotes species in the ice bulk. Finally, the prefix “i” is used when the total amount of ice species in the ice is considered (“i” = “g” + “b”). The CO ice is very abundant at the center of the core, reaching the fractional abundance of 40% w.r.t. water ice. At the location of the methanol peak, the fraction of CO ice is approximately twice smaller, and further drops to the edge of the core. In contrast to the model by A. I. Vasyunin et al. (2017), CO₂ is now abundant in the ice, reaching the fraction of 21% w.r.t. water ice at the location of the dust peak and 16% at the location of the methanol peak. Solid methanol is less abundant in the current model than in the model presented in A. I. Vasyunin et al. (2017). Its abundance is the highest in the center of the core (about 10% of solid water), and is decreasing toward the core edge, reaching 5% of solid water at the methanol peak. Nevertheless, methanol has larger abundance in our model than the average abundances reported in similar interstellar medium (ISM) objects (3% of water ice toward low-mass protostars, 4% toward high-mass protostars and cloud cores according to K. I. Öberg et al. 2011). However, M. Goto et al. (2021) reported the abundance of methanol ice equal to 11% of the water ice, consistent with our modeling results. Note however that the position of the background star (Source 3) used for the estimation of methanol ice abundance in M. Goto et al. (2021)

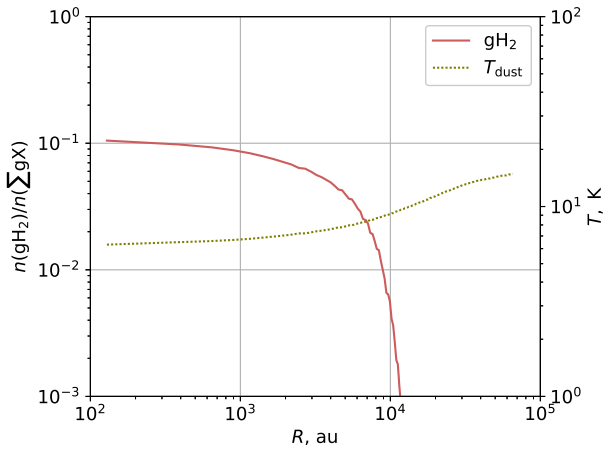


Figure 5. Fraction of molecular hydrogen on ice surface vs. radius. The value gets balanced almost instantaneously, and exhibits no appreciable changes throughout the simulation.

does not coincide neither with the dust peak nor with the methanol peak. The abundance of ammonia ice is approx. 30% larger than that of methanol ice, and follows the same radial trend. The abundance of solid methane is approximately similar at the locations of dust and methanol peaks: $\approx 2\%$ of water ice.

Such ice COMs as acetaldehyde, dimethyl ether, and formamide have abundances in the range of 10^{-8} – 10^{-7} at the dust peak (0.1% or less w.r.t. water ice). Methyl formate is the most abundant modeled COM in the ice. At the dust peak, its abundance amounts to 8.3×10^{-7} (1% w.r.t. water ice) and is comparable to methane ice abundance (which is 1.6×10^{-6}). Solid-phase acetaldehyde demonstrates some decrease toward the methanol peak, while the three other ice COMs have peaks toward the core edge.

In contrast to A. I. Vasyunin et al. (2017), where all the ice components have fractional abundances below 10^{-7} at the edge of the core, nonnegligible ice thickness is found now. In our simulations, the fractional abundance roughly corresponding to one surface monolayer is about 2×10^{-6} . At the core edge, water and carbon dioxide ices show the modeling abundances of 1.2×10^{-5} and 5.1×10^{-6} , correspondingly. This difference in ice thickness is likely due to the different Phase 1 of the simulation: now, we adopt a “translucent cloud” with the hydrogen number density of 10^3 cm^{-3} and the temperature linearly decreasing from 15 to 10 K, while previously it was a “diffuse cloud” with a smaller gas number density of 10^2 cm^{-3} and constant temperature of 20 K (the visual extinction is the same for both cases and equals 2 mag).

Molecular hydrogen amounts $\approx 10\%$ of total surface coverage at the central area of the core, with a decrease to the core edge (Figure 5). This results in a noticeable change of H and H_2 binding energies, which, in turn, affects both surface chemistry and RD rates. The high surface abundance of H_2 also enables chemical reactions with molecular hydrogen. As it is discussed below, such reactions are important for the formation of solid water and methane.

The time profiles for the COM abundances obtained with our GRD model at times relevant for the astrochemical modeling of starless cores are given in Appendix A.

3.4. Chemistry at the Methanol Peak with the GRD Model

In this section, the underlying chemical processes at the position of the methanol peak as observed at 4000 au are

discussed. All the numbers are given for the moment of the best agreement between the observed values and modeling results obtained with the GRD model.

It should be noted that diffusive reactions on the grain surface efficient at $T_{\text{dust}} \sim 10$ K, such as H-addition, also proceed efficiently in a nondiffusive mode. Thus, nondiffusive mechanisms effectively accelerate the rates of diffusive reactions at low temperatures. As an example, surface H-addition reactions forming COMs and methanol become about 20% faster due to the introduction of nondiffusive mechanisms. We now describe the main formation routes observed in our model for the following molecular species: CH_3OH , HCOOCH_3 , CH_3CHO , CH_3OCH_3 , NH_2CHO , and the major ice components H_2O , CO_2 , CH_4 , NH_3 .

CH_3OH . Methanol in the model is mainly produced on grains as a result of hydrogenation of CO molecules via the H-atom addition diffusive reactions presented in Table 7, Appendix B. This chain of reactions is also the main source of intermediate radicals, HCO, CH_2OH , and CH_3O , that play a key role in the formation of COMs via radical–radical chemical reactions that proceed nondiffusively (see below). The hydrogen abstraction reactions that are now included in the CO hydrogenation sequence increase the surface production of those radicals. The reactions also increase the abundance of methanol in the gas-phase by a factor of 2 in comparison to the test model run with hydrogen abstraction reactions switched off, because multiple acts of formation and destruction of CH_3O ultimately increase the probability of RD for methanol molecules. This is also true for its precursor species. The nondiffusive reaction $\text{gCH}_3\text{O} + \text{gCH}_3\text{O} \rightarrow \text{gCH}_3\text{OH} + \text{gH}_2\text{CO}$ accounts only for 4% of the surface methanol production.

One of the intermediates in the methanol formation chain, formaldehyde, can also be formed in our model via the reaction $\text{gC} + \text{gH}_2\text{O} \rightarrow \text{gH}_2\text{CO}$ (G. Molpeceres et al. 2021). However, its role was found to be negligible in producing formaldehyde ice, except for the outer edge of the core. The reaction also does not impact gas-phase formaldehyde abundance. Note, however, that, under the conditions of the translucent cloud where more atomic carbon is available, the nondiffusive version of this reaction produces most of gH_2CO at the early times of translucent cloud evolution. To the end of the translucent cloud phase in our simulations, the abundance of H_2CO ice amounts to $\approx 10^{-7}$, which is about an order of magnitude less than one ice monolayer.

Gas-phase processes account for 10% of methanol production. Among the major gas-phase routes, there is dissociative recombination of protonated or ionized COMs such as HCOOCH_3 and CH_3OCH_3 .

In L1544, the gas-phase methanol peak lies about 4000 au from the continuum “dust peak,” where CO is most heavily depleted. The major source of methanol in the gas-phase according to our model is RD of solid-state methanol during its formation on the surface of grain ice mantles. There, CH_3OH is formed via successive hydrogenation of CO molecules accreting from the gas. This hydrogenation must be completed while the reactants remain in the surface layer of ice; once they are buried in the bulk ice, RD can no longer occur. Thus, methanol ejected to the gas-phase is formed in reactions involving CO molecules that have only recently accreted onto the ice surface. The “methanol peak” therefore marks the radius where the accretion rate of CO is high, and atomic hydrogen on the surface is sufficiently abundant, not the region containing the largest reservoir of CO buried in the ice bulk.

HCOOCH₃. Almost all methyl formate, both in the gas-phase and in the icy mantles of grains, is surface formed. It is ejected to gas via RD. In our model, HCOOCH₃ is a product of the surface reaction $g\text{HCO} + g\text{CH}_3\text{O} \rightarrow g\text{HCOOCH}_3$ that proceeds nondiffusively. Its RD efficiency is 0.02%. The RD rate is calculated according to R. T. Garrod et al. (2007) and multiplied by the non-H₂O surface fraction, which equals 65% at $\approx 10^5$ yr and consists of 31% gCO and 15% gCO₂ at the methanol peak position. The RD efficiency of the reaction is effectively multiplied by a factor of ≈ 3 due to the hydrogen abstraction/addition loop $g\text{HCOOCH}_3 + \text{H} \rightarrow g\text{CH}_3\text{OCO} + \text{H}_2$; $g\text{CH}_3\text{OCO} + \text{H} \rightarrow \text{HCOOCH}_3$.

Although the gas-phase formation routes of methyl formate proposed in previous studies are also present in this work, their contribution is minor in comparison to the surface route. The reaction $\text{CH}_3\text{OCH}_2 + \text{O} \rightarrow \text{HCOOCH}_3 + \text{H}$, which was incorporated into astrochemical modeling by N. Balucani et al. (2015), contributes 0.4% of total HCOOCH₃ production rate. In A. I. Vasyunin et al. (2017), an important route of protonated methyl formate production is the reaction $(\text{CH}_3\text{OH})\text{H}^+ + \text{HCOOH} \rightarrow (\text{HCOOCH}_3)\text{H}^+ + \text{H}_2\text{O}$. In this work, the contribution of this reaction to the total formation rate of methyl formate is 0.1%.

CH₃OCH₃. Dimethyl ether in the model is mainly produced on grains via two channels. First is the reaction $g\text{CH}_3 + g\text{CH}_3\text{O} \rightarrow g\text{CH}_3\text{OCH}_3$ that proceeds nondiffusively. The probability of RD for dimethyl ether formed in this reaction is 0.03%. However, this value is further increased by a factor of ≈ 6 via the hydrogen abstractions/addition loop: $g\text{CH}_3\text{OCH}_3 + g\text{H} \rightarrow g\text{CH}_3\text{OCH}_2 + g\text{H}_2$; $g\text{H} + g\text{CH}_3\text{OCH}_2 \rightarrow g\text{CH}_3\text{OCH}_3$. The second channel is the nondiffusive reaction $g\text{CH}_2 + g\text{CH}_3\text{O} \rightarrow g\text{CH}_3\text{OCH}_2$ with the subsequent addition of a hydrogen atom. Thus, the second channel intervenes with the aforementioned hydrogen abstraction/addition loop by producing additional $g\text{CH}_3\text{OCH}_2$ radical. Therefore, the reaction $g\text{H} + g\text{CH}_3\text{OCH}_2 \rightarrow g\text{CH}_3\text{OCH}_3$ is not merely a part of a loop, but also a reaction responsible for the partial production of $g\text{CH}_3\text{OCH}_3$. Loop-amplified RD of surface-formed dimethyl ether is the major source of CH_3OCH_3 in the gas-phase, which accounts for 99% of its “production rate” in the gas.

Gas-phase processes account for less than 1% of dimethyl ether production. The most efficient gas-phase formation routes of dimethyl ether are the dissociative recombination of $(\text{CH}_3\text{OCH}_3)\text{H}^+$, which is in turn produced in the radiative association of CH_3OH and CH_3^+ ion, and neutral–neutral reaction $\text{CH}_3\text{O} + \text{CH}_3 \rightarrow \text{CH}_3\text{OCH}_3$. The role of those processes is suppressed in comparison to previous works. The formation of protonated dimethyl ether is less efficient than in, e.g., A. I. Vasyunin et al. (2017) because the abundance of gas-phase methanol in this work is significantly lower in comparison to that previous study. For the reaction $\text{CH}_3\text{O} + \text{CH}_3 \rightarrow \text{CH}_3\text{OCH}_3$, in this work, we adopt the “phase–space” reaction rate recently calculated in a detailed study by J. Tennis et al. (2021). This rate is an order of magnitude smaller than that used previously in N. Balucani et al. (2015) and A. I. Vasyunin et al. (2017). Therefore, the role of this reaction in formation of dimethyl ether is correspondingly reduced.

CH₃CHO. Gas-phase acetaldehyde is mainly produced in surface processes too. The major productive reaction is $g\text{CH}_3 + g\text{HCO} \rightarrow g\text{CH}_3\text{CHO}$ that proceeds nondiffusively.

The probability of RD for acetaldehyde formed in this reaction is 0.1%. The loop of H-addition/abstraction reactions $g\text{H} + g\text{CH}_3\text{CO} \rightarrow g\text{CH}_3\text{CHO}$ and $g\text{H} + g\text{CH}_3\text{CHO} \rightarrow g\text{H}_2 + g\text{CH}_3\text{CO}$ effectively increases the dust-to-gas acetaldehyde transfer rate by 10 times. Another route of $g\text{CH}_3\text{CO}$ and following $g\text{CH}_3\text{CHO}$ formation (approx. 25% of total production) is the chain $g\text{CO} \rightarrow g\text{CCO} \rightarrow g\text{HC}_2\text{O} \rightarrow g\text{CH}_2\text{CO} \rightarrow g\text{CH}_3\text{CO} \rightarrow g\text{CH}_3\text{CHO}$ experimentally verified by G. Fedoseev et al. (2022; and a similar chain for the bulk of grain mantles). The reactions of H-addition proceed diffusively with the acceleration by similar nondiffusive processes. The probability of RD for CH_3CHO formed in the last reaction of this chain is 0.1%. CCO is produced in the nondiffusive reaction $g\text{C} + g\text{CO} \rightarrow g\text{CCO}$. In the bulk, the nondiffusive reaction $b\text{O} + b\text{C}_2 \rightarrow b\text{CCO}$ is also efficient; however, its rate is 4 times lower than the rate of the reaction $b\text{C} + b\text{CO} \rightarrow b\text{CCO}$. At the methanol peak position, $b\text{CH}_2\text{CO}$ is efficiently produced via the photodissociation of ethanol ice by cosmic-ray photons.

In total, 98% of the delivery of acetaldehyde to the gas-phase is due to RD of acetaldehyde formed on the surface in the two reactions mentioned above. Gas-phase processes account for only about 2% of acetaldehyde production. The fastest gas-phase reaction with acetaldehyde as a product is the dissociative recombination of protonated acetaldehyde $(\text{CH}_3\text{CHO})\text{H}^+$. Protonated acetaldehyde is formed in the reaction $\text{H}_3\text{O}^+ + \text{C}_2\text{H}_2 \rightarrow (\text{CH}_3\text{CHO})\text{H}^+$. The reaction $\text{O} + \text{C}_2\text{H}_5 \rightarrow \text{CH}_3\text{CHO} + \text{H}$ also producing acetaldehyde is about 10 times slower than the dissociative recombination of $(\text{CH}_3\text{CHO})\text{H}^+$.

NH₂CHO. The gas-phase route of formamide formation $\text{NH}_2 + \text{H}_2\text{CO} \rightarrow \text{NH}_2\text{CHO} + \text{H}$ proposed in the OSU database (R. T. Garrod et al. 2008; V. Barone et al. 2015) was shown later to be inefficient (L. Song & J. Kästner 2016; K. M. Douglas et al. 2022). On the other hand, the efficiency of the surface formation route of formamide through the reaction $g\text{NH}_2 + g\text{HCO} \rightarrow g\text{NH}_2\text{CHO}$ has recently been confirmed experimentally (G. Fedoseev et al. 2016; K. J. Chuang et al. 2022). Therefore, in this study, this surface reaction is the only route to produce formamide. At low temperatures, it proceeds nondiffusively. The probability of RD for the NH_2CHO formed in this reaction is 0.02%. In our model, this is the only channel of delivery of formamide to the gas-phase in the cold environment of the prestellar core L1544.

According to the performed simulations, methyl formate is the most abundant COM in the ice. The nondiffusive reaction $g\text{HCO} + g\text{CH}_3\text{O} \rightarrow g\text{HCOOCH}_3$ and its bulk analog provide the major fraction of HCOOCH₃ ice. The combined rate of these reactions is 9 times faster than the total rate of the nondiffusive reaction $g\text{CH}_3 + g\text{HCO} \rightarrow g\text{CH}_3\text{CHO}$ and its bulk analog (both producing CH_3CHO ice) and 20 times faster than the total rate of the nondiffusive reaction $g\text{CH}_3 + g\text{CH}_3\text{O} \rightarrow g\text{CH}_3\text{OCH}_3$ and its bulk analog (both producing CH_3OCH_3 ice). Although all the reactions are barrierless, the abundances of the reactants differ significantly— 2.5×10^{-7} for gHCO (4.8×10^{-6} for bHCO), 7.9×10^{-8} for gCH₃O (2.2×10^{-6} for bCH₃O), and only 10^{-14} for gCH₃ (7.7×10^{-7} for bCH₃) at $\approx 10^5$ yr. As it was mentioned before, the ice radicals HCO and CH₃O are efficiently produced in the methanol formation chain. The CH₃ ice is mainly produced via the methoxy radical photodissociation reactions (including reactions with cosmic-ray-induced photons), along with the CH₃OH ice

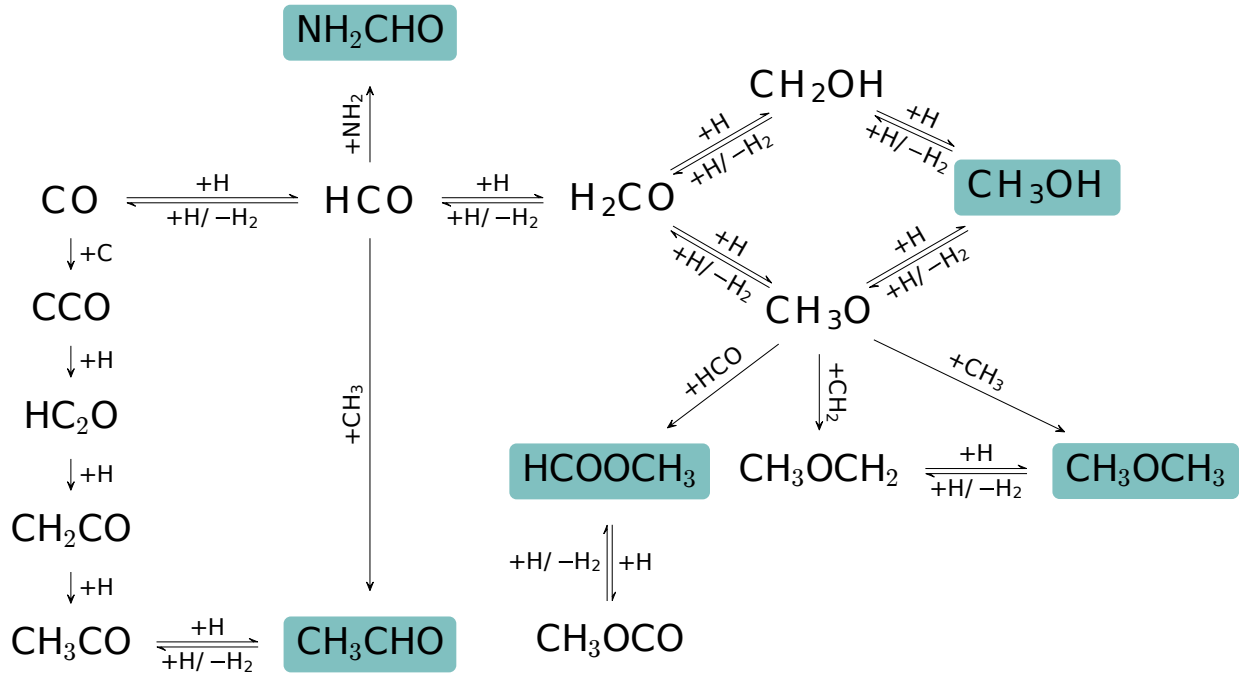


Figure 6. The major COM formation routes on grain surface. The COMs studied in our simulations have teal background. The species involved in the methanol formation chain are highlighted in bold. The chemical desorption in the COMs surface formation reactions is the main source of the gaseous COMs. The expressions $+H$ and $+H/-H_2$ together denote a pair of reactions, H-atom addition and H-atom abstraction.

photodissociation by cosmic-ray-induced photons and the diffusive reaction $gH_2 + gCH_2 \rightarrow gCH_3 + gH$. The contribution of the reaction $gH_2 + gCH \rightarrow gCH_3$ is minor. The production rates for CH_3 ice are significantly lower than those for the HCO and CH_3O ice radicals.

The main grain-surface paths of the COM formation are presented in Figure 6. In the gas, COMs appear due to RD during the final step of their formation.

Chemistry of main ice components. In this work, accretion of H_2 molecules on interstellar grains is considered. Given the large abundance of H_2 , it is not surprising that chemical reactions with it play an important role in the formation of some ice species. The most abundant ice is solid water, and the main gH_2O formation path is the diffusive reaction $gH_2 + gOH \rightarrow gH_2O + gH$, which accounts for 84% of surface water production at the position of the observational gas-phase methanol peak (Y. Oba et al. 2012). The nondiffusive H-atom abstraction reactions by OH radical from gH_2CO , $gHCO$, gCH_3O , and gCH_2OH account for 15% of gH_2O production in total. As for CO ice, like in many similar models, CO predominantly freezes out from gas.

CO_2 ice is produced on grains entirely due to nondiffusive processes. The main source of gCO_2 is the nondiffusive reaction $gOH + gCO \rightarrow gCO_2 + gH$ (89% of its total production rate). In our model, this reaction is a simplified representation for the two-step process $CO + OH \rightarrow HOCO$, $HOCO + H \rightarrow CO_2 + H_2$ (see D. Qasim et al. 2019). This channel remains significant even at larger radii, and despite photodissociation, the carbon dioxide ice maintains a nonnegligible abundance even at the core edge. Another channel is the nondiffusive reaction $gO + gHCO \rightarrow gCO_2 + gH$ (10%). The bulk analogs of the aforementioned reactions have rates about 5 times slower than the surface rates.

The source of gNH_3 is the diffusive reaction $gH_2 + gNH_2 \rightarrow gNH_3 + gH$ (99% of its production rate). This reaction has an activation barrier of ≈ 3000 K (J. Li &

H. Guo 2014). However, it is efficient due to a large abundance of H_2 on the surface and quantum tunneling of H_2 through the activation barrier. Although barrierless, the surface reaction $gH + gNH_2 \rightarrow gNH_3$ appears to be inefficient because of a low abundance of atomic hydrogen on the surface in comparison to the surface abundance of H_2 .

More than half of CH_4 is delivered to grain surfaces by a freeze-out from gas (65% of its formation rate) where it is formed in ion-molecule reactions. The main surface reaction producing gCH_4 is the diffusive reaction $gH_2 + gCH_3 \rightarrow gCH_4 + gH$ (34% of gCH_4 formation rate). gCH_3 is produced in a reaction $gCH_2 + gH_2 \rightarrow gCH_3 + gH$. In turn, the main formation route of gCH_2 is the reaction between hydrogen molecules and atomic carbon: $gC + gH_2 \rightarrow gCH_2$. Bulk diffusive and nondiffusive reactions $bH + bCH_3 \rightarrow bCH_4$ have rates similar to the rate of the aforementioned surface reaction producing gCH_4 .

3.5. Comparison to the Results and Chemistry with RD by M. Minissale et al. (2016b)

In the previous section, we presented the results of the GRD model that employs the parameterization of RD based on the RRKM theory and discussed in, e.g., R. T. Garrod et al. (2007). On the other hand, in the previous work where both the observed abundances of COMs as well as the location of the “methanol peak” in L1544 were simultaneously reproduced (A. I. Vasyunin et al. 2017), RD was parameterized differently. They employed an original parameterization of the results of laboratory experiments proposed in M. Minissale et al. (2016b). Generally, two mentioned parameterizations provide very different efficiencies of RD for the same reacting systems. Given the large uncertainty on the efficiency of RD for many reacting systems, we made a dedicated attempt to investigate the dependence of gas-phase COM abundances and ice composition on the chosen parameterization of RD. For that,

we constructed a model similar to the above-described GRD model but with the parameterization of RD following MRD. Below, it will be referred to as MRD model.

We ran the MRD model for the same conditions as GRD model described above. We explored different values of $E_{\text{diff}}/E_{\text{des}}$ for atomic and molecular species in both models (see Section 4.3 below for details). In our MRD model, no agreement for all species simultaneously has been found. Thus, for comparison with the GRD model, we have chosen the same $E_{\text{diff}}/E_{\text{des}}$ as in our main GRD model for the MRD model. The results were compared for the moment of time when the best agreement of the regular GRD model is achieved, i.e., 10^5 yr.

The results of the MRD model are presented in Figure 7. The abundances of gaseous methyl formate and dimethyl ether are lower than the observed values by about 1–2 orders of magnitude (Figure 7, top panels). Efficiencies of chemical desorption calculated according to MRD for the reactions $\text{gCH}_3 + \text{gCH}_3\text{O} \rightarrow \text{gCH}_3\text{OCH}_3$ and $\text{gHCO} + \text{gCH}_3\text{O} \rightarrow \text{gHCOOCH}_3$ are very low. Those are of the order of 10^{-7} and 10^{-14} correspondingly, w.r.t. corresponding surface reaction rates. H-addition surface reactions, which produce these COMs in loops, demonstrate similar RD efficiencies. Thus, in the case of MRD, surface processes cannot supply enough quantities of HCOOCH_3 and CH_3OCH_3 to the gas-phase to match observations. The abundance of acetaldehyde (CH_3CHO) is similar in the GRD and MRD models, because efficiencies of RD for surface formation routes of acetaldehyde are similar in both the GRD and MRD models. As for formamide, the efficiency of chemical desorption for the reaction $\text{gNH}_2 + \text{gHCO} \rightarrow \text{gNH}_2\text{CHO}$ is negligible in the MRD model. Thus, in the absence of efficient gas-phase production paths in both models, gaseous formamide exhibits abundances lower than 10^{-13} in the MRD model. The RD efficiencies for both the GRD and MRD models are given in Table 5. The shown calculated RD values are multiplied by the non- H_2O surface fraction, which is about 65% in the GRD model and 70% in the MRD model at the methanol peak position.

In contrast to the gas-phase, the ice composition does not experience dramatic variations with the change of the chemical desorption treatment. At the central parts of the core, all ice species exhibit changes in abundances within an order of magnitude compared to the ones obtained with GRD (Figure 7, middle and bottom panels). The most noticeable changes concern ices such as NH_3 , CH_4 , CH_3CHO , CH_3OCH_3 , and NH_2CHO , whose abundances become lower by about a factor of 2 in comparison to the model GRD. In particular, the chemical desorption for gNH_2 formation via the reaction $\text{gH} + \text{gNH} \rightarrow \text{gNH}_2$ is about 20 times more efficient in the model MRD than in model GRD. gNH_2 is a precursor of both gNH_3 and gNH_2CHO . Thus, in the model MRD, a larger fraction of gNH_2 is lost to the gas causing lower abundances of ammonia and formamide in the ice. The precursor of gCH_4 , CH_3OCH_3 , and gCH_3CHO – gCH_3 is formed more efficiently in the case of the model GRD. Its major production path is the reaction $\text{gH}_2 + \text{gCH}_2 \rightarrow \text{gCH}_3 + \text{gH}$, and the abundance of gCH_2 is greater in the case of the model GRD because the chemical desorption in its formation path $\text{gH}_2 + \text{gC} \rightarrow \text{gCH}_2$ is about 40 times less efficient for the model GRD than for the model MRD. Thus, unless the rates of chemical desorption are quite low compared to the rates of original surface reactions,

the changes in these rates may moderately affect the abundances of ice constituents too.

4. Discussion

In this work, we reproduced simultaneously the abundances of COMs observed in the L1544 prestellar core as well as the approximate location of the methanol peak w.r.t. the dust peak of the core. The modeled distance between the CH_3OH peak and the dust peak is somewhat larger than that observed (≈ 6000 au versus ≈ 4000 au). This difference may arise from the fact that we are assuming spherical symmetry while, in reality, L1544 is not spherically symmetric.

Moreover, our model presented in this study provides the composition of ices in L1544 that can be considered as more reasonable than in previous studies (e.g., A. I. Vasyunin et al. 2017): the fraction of methanol ice is close to the values obtained observationally by M. Goto et al. (2021) for L1544, and the fraction of CO_2 ice is similar to that obtained by the James Webb Space Telescope (JWST) for other dense dark clouds (see M. K. McClure et al. 2023). The modeled abundances of COMs in the ices are similar to the abundances of COMs in the gas-phase of hot cores/corinos (see, e.g., S. Bottinelli et al. 2004). The modeled abundances of icy COMs obtained in this study are compared to the corresponding gas-phase abundances in hot cores/corinos in Table 6. It can be seen that the abundances of icy COMs in most cases are equal to or higher than the abundances of organic molecules in the gas-phase of hot cores/corinos. It may imply that COMs observed in the gas-phase of later, more advanced stages of star formation, represented by hot cores/corinos, may already be formed during the earliest stages of protostellar development, in prestellar cores. Chemistry that proceeds in cold ices via nondiffusive mechanisms therefore appears to exhibit similar efficiency in the production of COMs as diffusive radical–radical chemistry that occurs in warm ($T > 30$ K) ices during the development of hot cores/corinos as proposed in R. Garrod et al. (2006). The smaller abundance of organic molecules in the gas-phase of hot cores compared to the ice of the cold core is consistent with the rapid destruction of COMs in gas-phase reactions upon sublimation. Untangling warm-up-driven and cold formation routes of COMs would require an isotopic analysis as proposed in J. K. Jørgensen et al. (2018). This is out of scope of this work.

In M. Jin & R. T. Garrod (2020), several nondiffusive mechanisms of surface reactivity are considered. Those are Eley–Rideal reactions, photodissociation-induced reactions, three-body reactions (we prefer to name them as “sequential reactions”), and three-body excited formation in addition to three-body reactions. In our GRD and MRD models, we employ all these types of nondiffusive processes, except for three-body excited reactions. We have also explored the individual impact of each of the aforementioned mechanisms. At low temperatures of prestellar cores, the role of Eley–Rideal reactions is found to be negligible. The impact of photodissociation-induced nondiffusive reactions on chemistry is significant. However, the model that includes only this type of nondiffusive reactivity is not capable of reproducing the observed quantities of HCOOCH_3 in the gas-phase: the modeled abundance of HCOOCH_3 is ≈ 1 order of magnitude lower than the observational values. In the ice, the abundance of methyl formate is >3 orders of magnitude

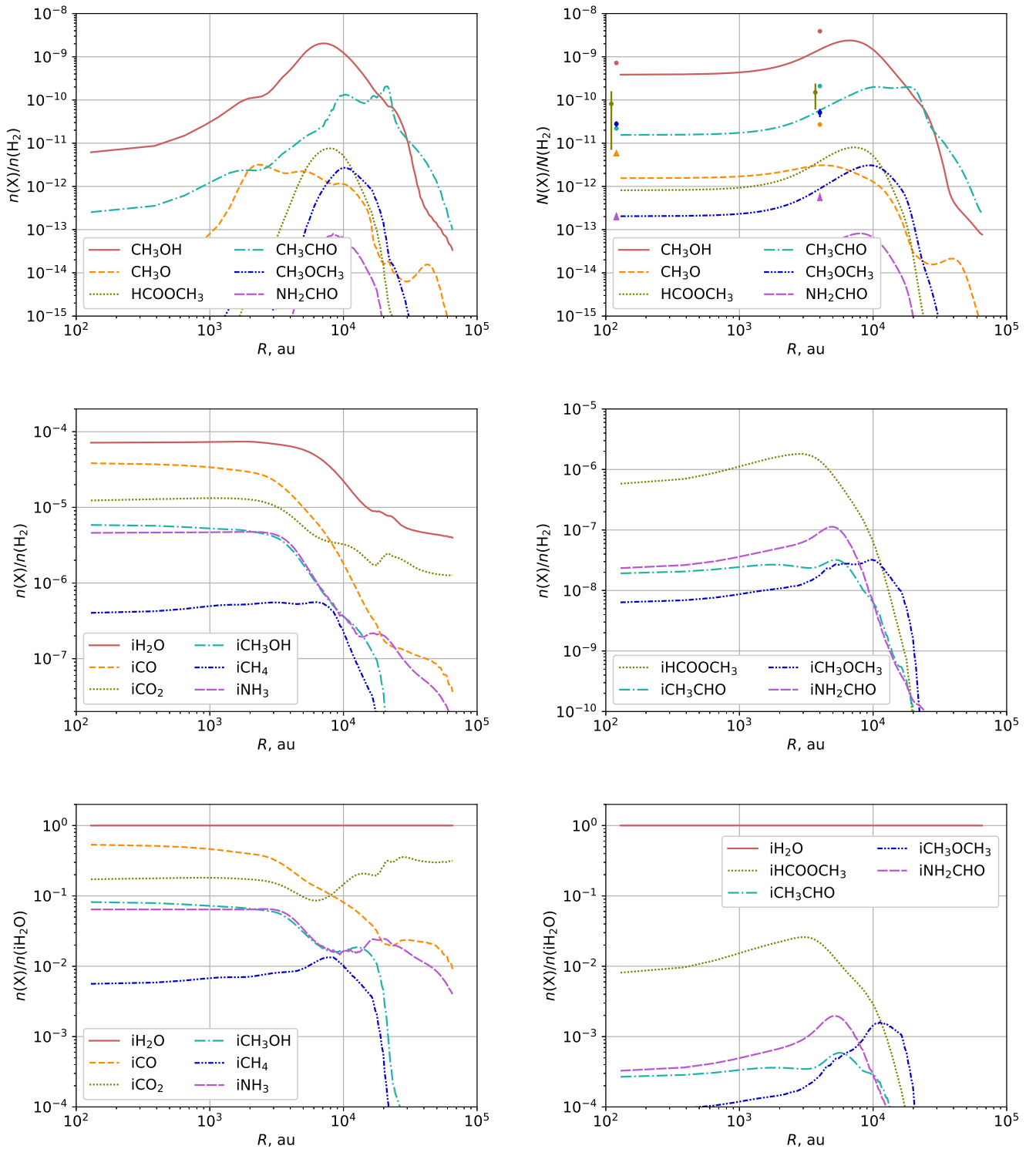


Figure 7. Radial profiles for the MRD model with reactive desorption treatment following M. Minissale et al. (2016b) at 10^5 yr. Top: profiles of modeled abundances (top left) and abundances derived as column density ratios (top right) of complex organic species. Abundances derived as column densities are smoothed over the $26''$ Gaussian beam. Middle: profiles of abundances of major ice constituents (middle left) and selected complex organic molecules in the ice (middle right) w.r.t. H_2 . Bottom: same as in the middle, but w.r.t. H_2O . Colored dots in the top right panel denote observational values by A. Chacón-Tanarro et al. (2019) for CH_3OH and by I. Jiménez-Serra et al. (2016) for other species, vertical lines are for error bars, and arrows are for observational upper limits.

lower than in our GRD model. In addition, the abundance ratio of solid CO_2 to H_2O drops to 5%. Thus, only the model that includes both photodissociation-induced reactions and sequential reactions matches all the observational data considered in this work, with the role of sequential reactions particularly important for the abundances of major ice

species. The introduction of excited three-body reactions (as defined in Section 2.5 in M. Jin & R. T. Garrod 2020) to our model worsens the agreement with observational data due to the overproduction of methyl formate. The details of this mechanism are particularly uncertain. Thus, it is not included in our GRD and MRD models.

Table 5

Reactive Desorption Efficiency (in Percentages of the Products Amounts) for the Most Important COMs Forming Reactions in the GRD and MRD Models

Reaction	GRD (%)	MRD (%)
$\text{gCH}_2\text{OH} + \text{gH} \rightarrow \text{gCH}_3\text{OH}$	0.05	0.03
$\text{gCH}_3\text{O} + \text{gH} \rightarrow \text{gCH}_3\text{OH}$	0.06	0.04
$\text{gHCO} + \text{gCH}_3\text{O} \rightarrow \text{gHCOOCH}_3$	0.02	$\sim 10^{-12}$
$\text{gCH}_3\text{OCO} + \text{gH} \rightarrow \text{HCOOCH}_3$	0.02	$\sim 10^{-12}$
$\text{gCH}_3 + \text{gCH}_3\text{O} \rightarrow \text{gCH}_3\text{OCH}_3$	0.03	$\sim 10^{-5}$
$\text{gCH}_3\text{OCH}_2 + \text{gH} \rightarrow \text{gCH}_3\text{OCH}_3$	0.04	$\sim 10^{-4}$
$\text{gCH}_3 + \text{gHCO} \rightarrow \text{gCH}_3\text{CHO}$	0.1	0.05
$\text{gCH}_3\text{CO} + \text{gH} \rightarrow \text{gCH}_3\text{CHO}$	0.1	0.07
$\text{gNH}_2 + \text{gHCO} \rightarrow \text{gNH}_2\text{CHO}$	0.02	$\sim 10^{-6}$

Note. In both GRD and MRD cases, the calculated RD values are already multiplied by the non-H₂O surface fraction.

4.1. COMs versus Methanol

We compared our GRD model gas-phase COM abundances convolved with the 26'' beam to the COM abundances reported in observations toward cold cores (see Figure 8). We also show COMs-to-CH₃OH column density ratios. The abundances of COMs and methanol toward L1544, L1498, L1517B, L1521E (Taurus MC), L1689B (Ophiuchus MC), L183 are in agreement with the abundances predicted by our model for L1544, showing larger and smaller values within an order of magnitude of the model results (see caption of Figure 8 for the references). The abundances of CH₃OH, CH₃CHO, CH₃OCH₃ toward B5 and cores 67–800 (Perseus MC) are systematically higher than the modeled ones. This may be a scale effect, which is a combination of $\approx 60''$ beam and ≈ 300 pc distance to Perseus (the beam covers ≈ 18000 au) compared to $\approx 30''$ beam and ≈ 130 pc distance to the other cores (the beam covers ≈ 3900 au). This means that the abundances toward the Perseus cores should be compared with the model values for the methanol peak rather than dust peak, and then, the observation results agree with the simulations. Another possibility is the higher density of the cloud surrounding the Perseus cores (which mostly reside in the region of clustered star formation NGC 1333) compared to the relatively isolated L1544, L1498, L1517B, L1521E, L1689B, L183 cores. However, in cold cores and other evolutionary states (including comets), COM abundance w.r.t. CH₃OH varies roughly within an order of magnitude (see, e.g., S. Scibelli et al. 2024). This strongly hints for similar chemical evolution between different stages of low-mass star formation.

4.2. Comparison to A. I. Vasyunin et al. (2017) and the Importance of Tunneling through Diffusion Barriers

The results obtained with our model MRD could not reproduce the observed abundances of COMs in the gas-phase of L1544. This, to some extent, contradicts the previous results obtained with the unmodified diffusive code presented in A. I. Vasyunin et al. (2017). The RD of several nondiffusively formed COMs from grains is negligible in both A. I. Vasyunin et al. (2017) and the MRD model. On the other hand, the gas-phase COM formation routes proposed in A. I. Vasyunin et al. (2017) are still included in the MRD model. This discrepancy

originates from the introduction of newly constrained values for reaction rates into the MRD model following recent laboratory and theoretical data. Those updates largely explain the fact that MRD model is not capable of reproducing the observed abundances of COMs in L1544.

In the best-fit model presented in A. I. Vasyunin et al. (2017), gas-phase chemistry of methanol plays a key role in the formation of both formaldehyde and dimethyl ether. Methanol has an abundance of 2.7×10^{-8} at the location of the methanol peak. In the model MRD, the gas-phase abundance of methanol is 2×10^{-9} . This renders the efficiency of gas-phase chemistry responsible for the formation of O-bearing COMs in A. I. Vasyunin et al. (2017). The lower abundance of gas-phase methanol in the MRD model in comparison to A. I. Vasyunin et al. (2017) is due to the following differences between the models. First, there is a difference in the widths of the activation barriers in the reactions $\text{H} + \text{CO} \rightarrow \text{HCO}$ and $\text{H} + \text{H}_2\text{CO} \rightarrow \text{CH}_2\text{OH}/\text{CH}_3\text{O}$: 1.35 Å; see Table 7 of Appendix B versus 1.2 Å in A. I. Vasyunin et al. (2017). This makes surface hydrogenation of CO to CH₃OH slower, reducing its grain-to-gas transfer rate via RD. Second, hydrogen abstraction loops introduced for the intermediate steps of the CO hydrogenation sequence in this work further reduce the efficiency of CH₃OH formation on the surface and CH₃OH transfer to the gas-phase. Importantly, switching on tunneling for diffusion of H and H₂ does not help to improve the agreement between the results of the MRD model and observed values. Another key discrepancy with the reaction rates used by A. I. Vasyunin et al. (2017) is the implementation of the recent estimate for the $\text{CH}_3 + \text{CH}_3\text{O} \rightarrow \text{CH}_3\text{OCH}_3 + h\nu$ reaction rate proposed by J. Tennis et al. (2021). This rate is an order of magnitude lower than the value used in A. I. Vasyunin et al. (2017). The factors listed above made the MRD model not capable of explaining gas-phase abundances of COMs in L1544 in contrast to the model presented in A. I. Vasyunin et al. (2017).

Note also that the abundance of solid methanol in A. I. Vasyunin et al. (2017) reaches 40% w.r.t. water ice, while in this work its abundance is about four times smaller. The overproduction of solid methanol in A. I. Vasyunin et al. (2017) can be partially explained by the lack of efficient mechanisms for the competitive reactions resulting in the formation of CO₂ ice from CO molecules. Indeed, the diffusive surface reactions $\text{CO} + \text{OH} \rightarrow \text{CO}_2 + \text{H}$ and $\text{CO} + \text{O} \rightarrow \text{CO}_2$ are not efficient at dust temperatures of ≤ 10 K in A. I. Vasyunin et al. (2017) because their model lacks nondiffusive reaction mechanisms and has a diffusion-to-binding energy ratio for molecules set to a moderately high value of 0.5. Implementation of nondiffusive reaction mechanisms is required to produce observed amounts of CO₂ ice under such conditions.

The better agreement of our GRD model results with the observations compared to the results by A. I. Vasyunin et al. (2017) is also explained by different formation routes for COMs. In our simulations, COMs predominantly form on dust grains in nondiffusive radical–radical reactions (CH₃CHO also forms in the chain suggested by G. Fedoseev et al. 2022), arriving at the gas via efficient chemical desorption (R. T. Garrod et al. 2007), enhanced by H-addition/abstraction loops. In A. I. Vasyunin et al. (2017), COMs were predominantly produced in gas-phase reaction chains involving CH₃OH as a precursor. COM abundances were strongly

Table 6Comparison of the Modeled Abundances of Ice COMs in L1544, $n(X)$, and the Observational Abundances of These COMs in the Gas-phase of Hot Cores/Corinos

	CH ₃ OH	CH ₃ CHO	CH ₃ OCH ₃	HCOOCH ₃	Reference
			<i>ice COMs in L1544</i>		
Dust Peak	7.5×10^{-6}	7.3×10^{-8}	1.8×10^{-8}	8.3×10^{-7}	This study, modeled
CH ₃ OH Peak	3.3×10^{-6}	4.5×10^{-8}	5.4×10^{-8}	1.7×10^{-6}	This study, modeled
			<i>gas-phase COMs in hot cores/corinos</i>		
IRAS 4A	$\leq 7.0 \times 10^{-9}$...	$\leq 2.8 \times 10^{-8}$	7.0×10^{-8}	S. Bottinelli et al. (2004)
IRAS 4A2	...	$1.1\text{--}7.4 \times 10^{-9}$	1.0×10^{-8}	1.1×10^{-8}	A. López-Sepulcre et al. (2017)
IRAS 16293	3.0×10^{-7}	5.1×10^{-8}	2.4×10^{-7}	4.0×10^{-7}	S. Cazaux et al. (2003)
OMC-1	1.0×10^{-7}	...	8.0×10^{-9}	2.0×10^{-8}	E. C. Sutton et al. (1995)
	1.0×10^{-6}	6.0×10^{-10}	...	9.0×10^{-8}	M. Ikeda et al. (2001)
VLA 3	6.1×10^{-8}	3.3×10^{-9}	C. Gieser et al. (2019)
SVS13-A	3.0×10^{-8}	4.0×10^{-9}	5.0×10^{-8}	4.0×10^{-8}	E. Bianchi et al. (2019)
IRAS4B	7.0×10^{-7}	...	$< 1.2 \times 10^{-6}$	1.1×10^{-6}	S. Bottinelli et al. (2007)
IRAS2A	3.0×10^{-7}	...	3.0×10^{-8}	$< 6.7 \times 10^{-7}$	S. Bottinelli et al. (2007)
HOPS 373SW	9.0×10^{-8}	2.2×10^{-9}	...	1.7×10^{-8}	J.-E. Lee et al. (2023)

dependent on methanol abundance, and their COM-to-methanol ratios were lower than ours.

Interestingly, partial grain-to-gas transfer is a key mechanism regardless of whether gas-phase or grain-surface chemistry is responsible for the formation of COMs in prestellar cores. In the first case, RD delivers precursors of COMs to the gas. In the second case, if COMs are formed on grains, they shall be somehow delivered to the gas. In cold, dark, and dense environments of prestellar clouds, RD is a promising candidate to explain this delivery.

4.3. The Impact of Different $E_{\text{diff}}/E_{\text{des}}$ Ratios

The exact ratio between diffusion energy and desorption energy is still debatable. Experiments and models suggest many different values for the ratio of diffusion energy to desorption energy. D. P. Ruffle & E. Herbst (2000) used $E_{\text{diff}}/E_{\text{des}} = 0.77$ in their simulations. In M. Ruaud et al. (2016) and V. Wakelam et al. (2017), all species including H and H₂ are assumed to diffuse by thermal hopping only, with $E_{\text{diff}}/E_{\text{des}} = 0.4$.

More detailed models published so far include different values of diffusion-to-desorption energy ratios for individual species. For example, K. Acharyya (2022) summarized the desorption and diffusion energies for CO from a number of experiments, and explored the impact of E_b/E_D ratios varied in a range of 0.1–0.5 for CO, and in a range of 0.3–0.5 for other species, on the results of astrochemical modeling. They found that models with higher diffusion barriers provide a relatively better agreement with the observational data compared to models with lower diffusion barriers. K. Furuya et al. (2022) found no clear relation between E_b and E_D , an Amorphous Solid Water ice. According to their study, the E_b/E_D ratio may vary in a range of 0.2–0.7, depending on a species. Moreover, binding and probably diffusion energies of species may also depend on surface coverage by the species (see, e.g., J. He et al. 2016a). Finally, on a microscopic level, each surface binding site is characterized by its own value of binding energy, and thus, a distribution of binding and diffusion energies on the surface shall take place (see, e.g., T. Grassi et al. 2020; K. Furuya 2024). However, such a level of detail is normally not implemented in models based on rate equations:

in this work, we consider only two values of E_b/E_D for adsorbed species, one for atoms and another for molecules.

In order to explore how well the simulations with various $E_{\text{diff}}/E_{\text{des}}$ ratios reproduce the observational data, we run two sets of models, using models GRD and MRD, with $E_{\text{diff}}/E_{\text{des}}$ values in an interval of 0.30–0.60 and a step of 0.05, and with disabled tunneling for diffusion. The $E_{\text{diff}}/E_{\text{des}}$ ratios for atomic and for molecular species have been varied separately. The simulations with MRD do not provide any combinations of atomic and molecular $E_{\text{diff}}/E_{\text{des}}$ ratios with which the model reproduces the observational data well. The results of the simulations with GRD are summarized in Figure 9. Each cell in Figure 9 represents a particular pair of molecular and atomic $E_{\text{diff}}/E_{\text{des}}$ values. A cell is colored in green if the nondiffusive model with a given $E_{\text{diff}}/E_{\text{des}}$ reproduces the observed abundances of COMs in the gas-phase. Blue colored cells indicate models that do not reproduce the observational data. Yellow color indicates the pairs of $E_{\text{diff}}/E_{\text{des}}$ values where both the diffusive (with nondiffusive reactions switched off) and nondiffusive models reproduce the observational gas-phase values well (see Appendix C). In the case of Figure 9, we consider that a model reproduces observational data well if a time moment t exists at which the modeled CO depletion factor is within a factor of 2 compared to the observational value, and modeled abundances of all six studied gas-phase species are *in agreement* with observed values simultaneously at the locations of dust and methanol peaks.

As seen in Figure 9, the atomic $E_{\text{diff}}/E_{\text{des}}$ values have in general more effect on species' abundances than the molecular $E_{\text{diff}}/E_{\text{des}}$. With the increase of atomic $E_{\text{diff}}/E_{\text{des}}$ ratios grows the reproducibility of the observational data. For the atomic $E_{\text{diff}}/E_{\text{des}}$ values of 0.55–0.60, nondiffusive models reproduce the observational data well with any molecular $E_{\text{diff}}/E_{\text{des}}$ ratio. However, the relevance of such high $E_{\text{diff}}/E_{\text{des}}$ ratios is limited by the bulk composition. In our main model (where $E_{\text{diff}}/E_{\text{des}}$ is 0.5 for atomic species and 0.3 for molecular species), the abundance of unreacted H atoms entrapped in bulk ice is 10^{-7} at the dust peak, whereas increasing the atomic $E_{\text{diff}}/E_{\text{des}}$ only to 0.55 leads to the growth of H bulk abundance up to 2.4×10^{-6} . The situation is similar for diffusive models. Thus, we assumed the atomic $E_{\text{diff}}/E_{\text{des}}$ value 0.5 to be more acceptable than the larger ones.

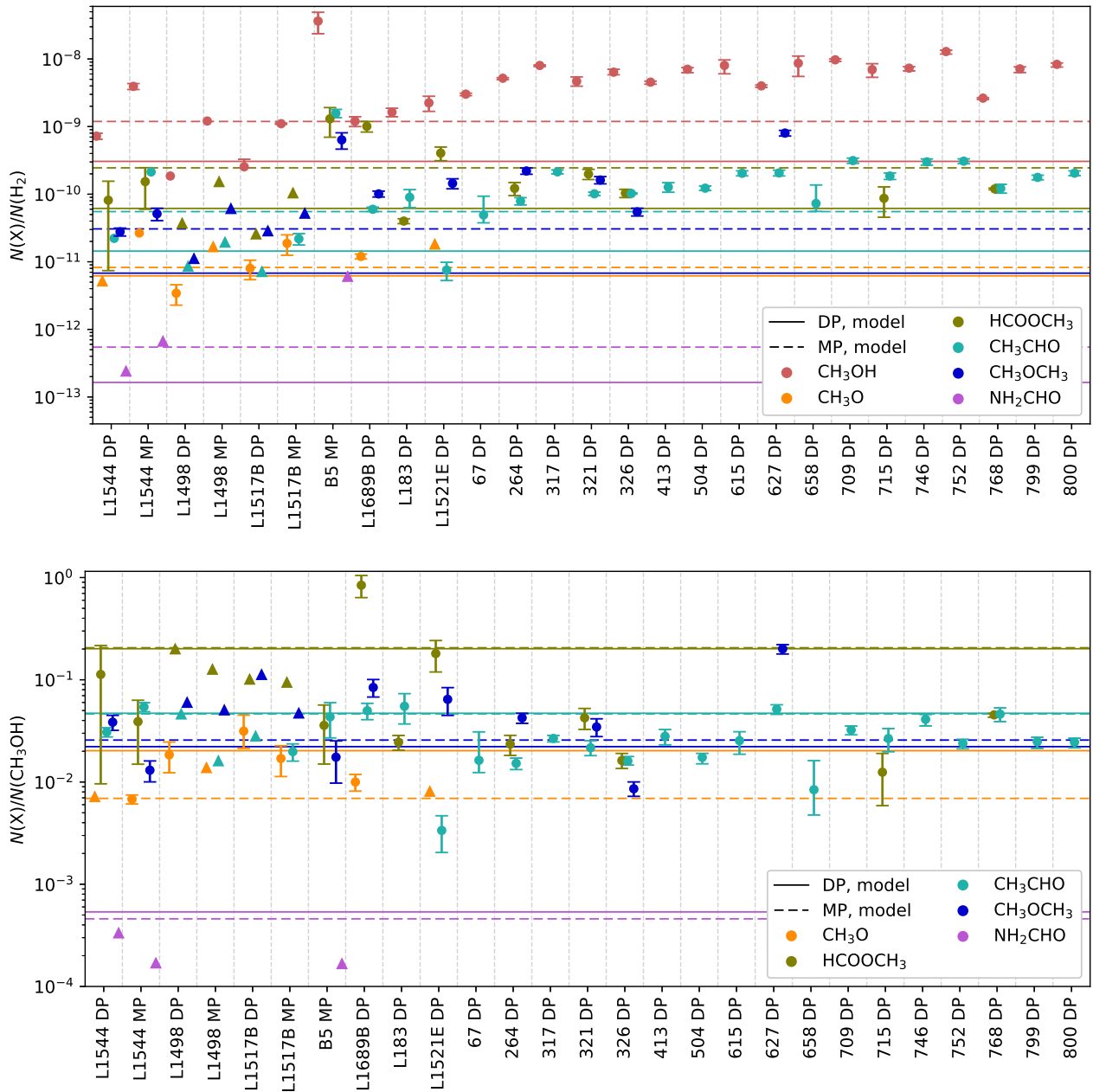


Figure 8. Top: COM observational abundances in cold cores in comparison with the abundances obtained as column densities ratios with our GRD model for the prestellar core L1544. Bottom: same for COMs-to- CH_3OH column densities ratios. (Note that the physical model of L1544 may not be representative of other sources in this comparison.) Circles denote observational values with error bars; triangles denote observational upper limits. DP is for the dust peak; MP is for the methanol peak. The modeled species abundances and ratios are given with horizontal lines of corresponding colors. The observational data is collected from I. Jiménez-Serra et al. (2016), L1544; A. Chacón-Tanarro et al. (2019), L1544; methanol; S. Spezzano et al. (2016), L1544, methanol (peak); I. Jiménez-Serra et al. (2021), L1498; A. Megías et al. (2023), L1517B; V. Taquet et al. (2017), B5; E. S. Wirstrom et al. (2014), B5, $N(\text{H}_2)$; A. Bacmann et al. (2012), L1689B; A. Bacmann & A. Faure (2016), L1689B, methanol and methoxy radical, L1521E, methoxy radical; V. Lattanzi et al. (2020), L183; Z. Nagy et al. (2019), L1521E, methanol; S. Scibelli et al. (2021), L1521E, methyl formate, acetaldehyde, dimethyl ether; S. Scibelli et al. (2024), cores 67–800 in Perseus.

With the atomic $E_{\text{diff}}/E_{\text{des}}$ value of 0.5, the ice composition (both main ice components and COMs) remains nearly stable when varying the molecular $E_{\text{diff}}/E_{\text{des}}$ value. At the central area of the core, abundance variations for the time moment of 10^5 yr do not exceed one-tenth of an order of magnitude. However, in the models with molecular $E_{\text{diff}}/E_{\text{des}} \geq 0.4$, the modeled gas-phase abundances for the dust peak fit the observational values only in the narrow time interval of $\approx 2.0 \times 10^4$ – 4.0×10^4 yr, when the gaseous CO abundance is still higher than 2.0×10^{-5} , and thus, the observed CO

depletion factor is not attained. Thus, we discard these models and employ $E_{\text{diff}}/E_{\text{des}} = 0.3$ for molecular species.

4.4. Sticking Coefficient

Several numerical and laboratory studies assess the temperature-dependent sticking coefficient for light species H and H_2 (e.g., D. Hollenbach & E. E. Salpeter 1970; K. Masuda & J. Takahashi 1997; A. Al-Halabi & E. F. van Dishoeck 2007; E. Matar et al. 2010; S. Cazaux et al. 2011; K. Acharyya 2014; V. K. Veeraghattam et al. 2014; J. He et al. 2016b) and heavier

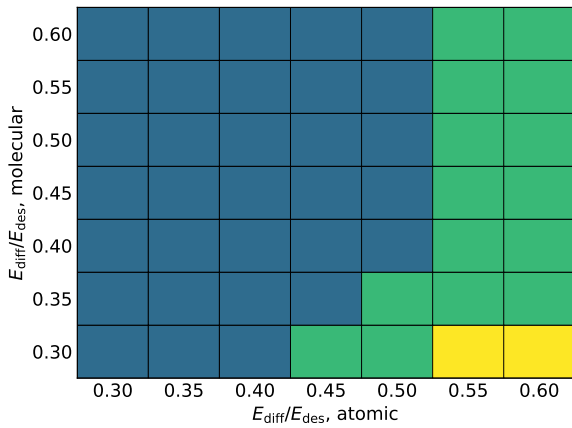


Figure 9. The generalizing diagram of the success of different models in reproducing observed values of gas-phase abundances of complex organic species in the L1544 prestellar core. Blue: models do not reproduce the observational data. Green: nondiffusive models reproduce the observations. Yellow: both nondiffusive and diffusive models reproduce the observations.

molecules such as N_2 , O_2 , and CO (e.g., K. I. Öberg et al. 2005; S. E. Bisschop et al. 2006; G. W. Fuchs et al. 2006).

The H-atom sticking coefficient is difficult to measure in laboratory conditions. The classical molecular dynamics simulations by V. K. Veeraghattam et al. (2014) on an amorphous ice substrate predict the sticking probability of H atoms in the range of 0.7–1.0 for the temperature of the amorphous ice substrate of 10 K and the incident energy of 100 K (Figure 4 in their paper). The calculations by V. Buch & Q. Zhang (1991) claimed 0.85 for H atoms.

In our simulations, sticking probabilities are equal to unity for all species except H. For atomic hydrogen, sticking probability is calculated according to D. Hollenbach & C. F. McKee (1979) and equals ≈ 0.8 at 10 K dust temperature.

4.5. Sputtering by Cosmic Rays

In this work, we found that, in order to match the observed values of abundances of COMs in the gas-phase of L1544, one has to employ treatment of RD that yields desorption probability upon formation for COMs of $\sim 0.1\%$. That is consistent with the RD treatment based on RRKM theory proposed in R. Garrod et al. (2006). However, there are other types of nonthermal desorption that could be efficient for COMs. Recently, the experimental works by E. Dartois et al. (2018, 2020, 2021) provided the yields for sputtering by cosmic rays for some abundant ices, including water, carbon monoxide, carbon dioxide, and methanol. Similarly to the approach suggested in V. Wakelam et al. (2021), we implemented sputtering by cosmic rays into our modeling as a type of desorption. The sputtering rate has been calculated taking into account the fractions of CO and CO_2 ices on the surface and in the bulk, and for the rest of the mantle, the parameters for H_2O ice have been used.

In our simulations, the only significant effect of sputtering appeared to be an enhancement of abundances of gaseous COMs toward the prestellar core center, typically within 1 order of magnitude (CH_3OH , from 7.8×10^{-13} to 3.4×10^{-12} ; $HCOOCH_3$, from 5.0×10^{-14} to 2.4×10^{-13} ; CH_3CHO , from 6.2×10^{-14} to 1.9×10^{-13} ; CH_3OCH_3 , from 2.8×10^{-16} to 1.6×10^{-15} ; NH_2CHO , from 1.9×10^{-18} to 3.6×10^{-16}). However, this does not affect the abundances calculated as

column densities $N(X)/N(H_2)$, which we use for the comparison with the observations. This result is somewhat in agreement with the conclusion of V. Wakelam et al. (2021), who suggest that, at high densities, sputtering by cosmic rays dominates the desorption for molecules formed on dust grains, such as CH_3OH and CH_3OCH_3 . In our simulations, though, this effect becomes noticeable for gas densities higher than $\approx 3 \times 10^5 \text{ cm}^{-3}$, while V. Wakelam et al. (2021) state $4 \times 10^4 \text{ cm}^{-3}$ as a reference point. It should be noted that their and our chemical models significantly differ from each other; for example, their model includes the chemistry of Van Der Waals complexes (M. Ruaud et al. 2015) and does not include nondiffusive chemistry. Ice COMs and main ice constituent abundances in our simulations remain the same as without sputtering.

5. Conclusions

In this study, we performed chemical modeling of the formation and evolution of COMs and icy mantles of interstellar grains in the prestellar core L1544. For that, we utilized an updated version of the MONACO code, which now includes basic treatment for nondiffusive mechanism of surface chemical reactivity, surface reactions with H_2 molecules, H-atom induced abstraction routes, as well as some recent important updates on gas-phase and surface chemical processes. The most important results may be summarized as follows.

1. The updated MONACO code, with the inclusion of the treatment for nondiffusive chemical reactivity in icy mantles of interstellar dust grains and the reaction network updated with the most recent laboratory and theoretical results, provides results that demonstrate a very good agreement with the observational data on COMs in the prestellar core L1544. It also provides a reasonable composition of icy mantles in the core, which is in agreement with the observations of L1544 and similar interstellar objects. For the first time, both the abundances of COMs in the gas-phase and the location of methanol peak in L1544 are successfully reproduced with a model that includes nondiffusive chemical reactivity.
2. The mechanism of nondiffusive reactivity of radicals proposed in G. Fedoseev et al. (2015) and S. Ioppolo et al. (2021) is implemented in the MONACO code following M. Jin & R. T. Garrod (2020). It appears to be efficient in producing COMs in icy mantles of cold ($T_{\text{dust}} < 10 \text{ K}$) interstellar grains with abundances 0.1%–3% with respect to (w.r.t.) water ice. Importantly, abundances of COMs in the ice are similar to the gas-phase abundances of those species observed in hot cores/corinos. This supports a scenario where COMs observed in the gas of hot cores are formed earlier than the warm-up transition phase from cold prestellar cores to hot cores/corinos occurs.
3. We found that parameterization of the efficiency of chemical desorption utilized in the model strongly affects the abundances of COMs in the gas-phase, but only moderately—the abundances of both simple and complex species—in ices. Thus, the formation of COMs in ices and delivery of COMs to the cold gas of prestellar cores may be considered as two separate problems. As shown in this study, the fraction of surface-formed COMs needed to be transferred to the gas upon

formation to match observed abundances is $\sim 0.1\%$. In our model, such a desorption rate for complex molecules is only achieved with RD with rates calculated following the RRKM theory. Neither cosmic-ray-induced sputtering implemented following V. Wakelam et al. (2021) nor the RD parameterization proposed in MRD has the similar efficiency for COMs.

Acknowledgments

The authors wish to thank the anonymous referees for valuable comments, which helped us to improve the manuscript. This research has made use of NASA's Astrophysics Data System. K.B., G.F. and A.V. acknowledge the support of the Russian Science Foundation via the Project 23-12-00315 and Russian Ministry of Science and Higher Education via the project FEUZ-2025-0003 (Appendix C). G.F. also benefited from the Xinjiang Tianchi Talent Program (2024). I.J.-S. acknowledges funding from grant PID2022-136814NB-I00

funded by the Spanish Ministry of Science, Innovation and Universities/State Agency of Research MICIU/AEI/10.13039/501100011033 and by "ERDF/EU," and from the ERC grant OPENS (project number 101125858) funded by the European Union. Views and opinions expressed are however those of the author(s) only and do not necessarily reflect those of the European Union or the European Research Council Executive Agency. Neither the European Union nor the granting authority can be held responsible for them.

Appendix A

Time Dependence of molecular abundances

Modeled abundances of species evolve significantly with time. In Figure 10, temporal evolution of abundances of gaseous COMs considered in this study is presented. Note that abundances at early time of 10^4 years depend strongly on the assumed initial chemical composition in the model.

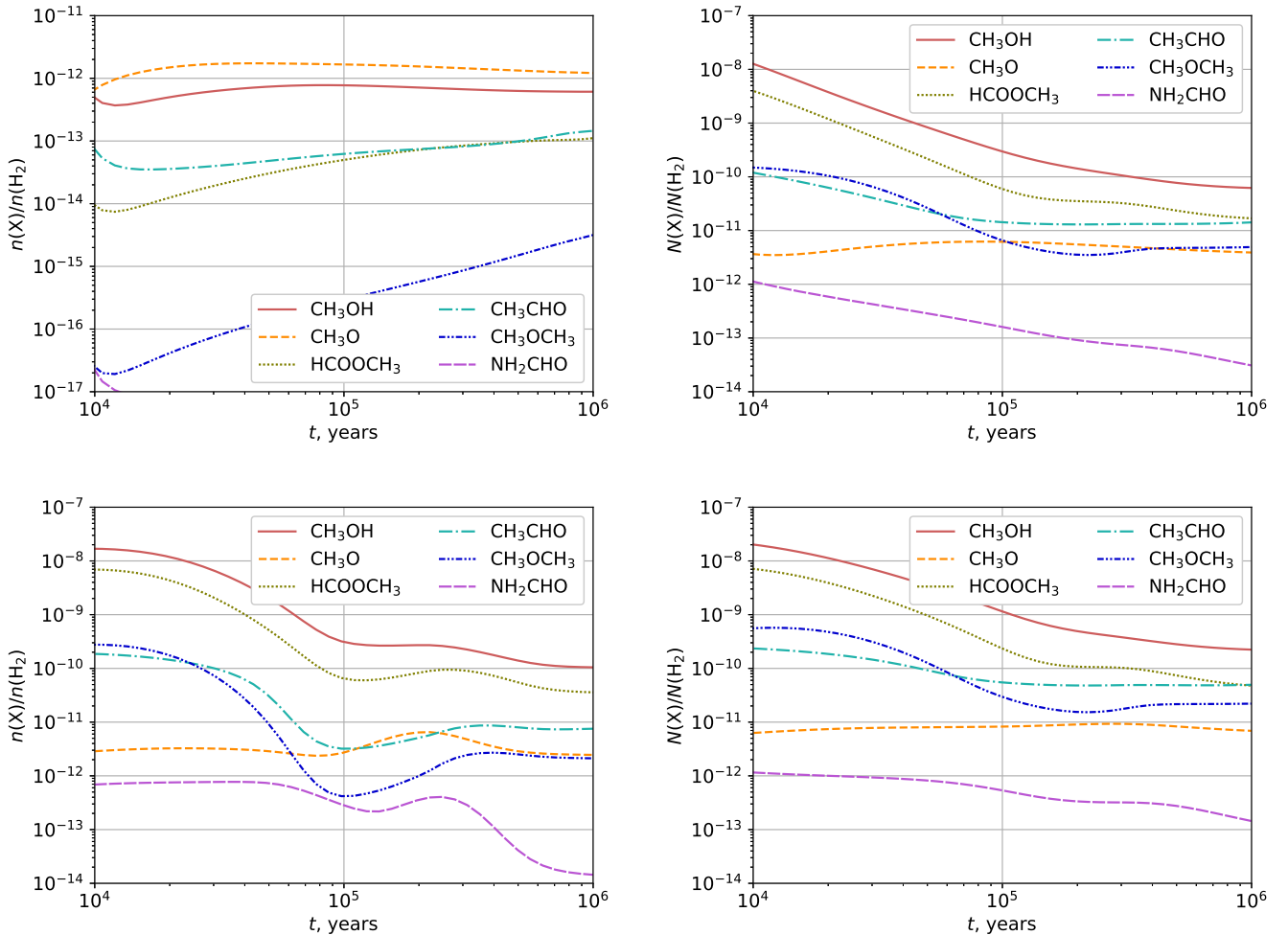


Figure 10. Time profiles of COM abundances obtained with our GRD model for the prestellar core L1544. Top: profiles of modeled abundances for the dust peak (top left) and abundances derived as modeled column density ratios for the dust peak (top right). Abundances derived as column densities are smoothed over the $26''$ Gaussian beam. Bottom: same as in the top, but for the methanol peak position, 4000 au. (Note different abundance scale for the top left image.)

Appendix B Updates to the Chemical Network

The network of chemical reactions used in this study is mainly based on that presented in I. Jiménez-Serra et al. (2021). However, a number of important updates are introduced to this network following recent experimental studies and theoretical findings.

First, chemistry of CO hydrogenation on the grain surface has been extended. Hydrogen addition reactions that lead to the gradual hydrogenation of CO into methanol (CH_3OH) through several intermediates (HCO , H_2CO , $\text{CH}_3\text{O}/\text{CH}_2\text{OH}$) were complemented by hydrogen abstraction reactions following M. Jin & R. T. Garrod (2020; see Table 7). We also included a reaction between methoxy radical and formaldehyde producing methanol ($\text{gCH}_3\text{O} + \text{gH}_2\text{CO} \rightarrow \text{gCH}_3\text{OH} + \text{gHCO}$) with a barrier of 2670 K proposed in S. Álvarez-Barcia et al. (2018); recently, the reaction was experimentally confirmed by J. C. Santos et al. (2022).

Recently, G. Molpeceres et al. (2021) showed that formaldehyde (H_2CO), a species that can be converted to methanol via two subsequent additions of hydrogen atoms, can be formed in a reaction $\text{gC} + \text{gH}_2\text{O} \rightarrow \text{gH}_2\text{CO}$. This reaction may occur efficiently before the “catastrophic freeze-out” of CO on grains (P. Caselli et al. 1999), thus facilitating chemistry of methanol and other COMs on earlier stages of formation of prestellar cores. Given the two-stage nature of our model (see Section 2.2), we included this reaction in the chemical network.

Second, formation routes for other COMs have been updated. As a route of acetaldehyde formation, we included the reaction chain proposed by G. Fedoseev et al. (2022; see Figure 3 in their paper). Table 8 contains reactions from the chain leading to solid acetaldehyde. Recent theoretical results by S. Ferrero et al. (2023) suggest that acetaldehyde ice can possibly form in the conditions similar to those of ISM via successive hydrogenation of iced ketene CH_2CO (helped by H tunneling through the reaction barrier) and then the acetyl radical CH_3CO . In the previous work by A. I. Vasyunin et al. (2017), acetaldehyde is mainly formed in the gas-phase reaction $\text{CH} + \text{CH}_3\text{OH} \rightarrow \text{CH}_3\text{CHO} + \text{H}$. The rate constants for this reaction were taken from D. G. Johnson et al. (2000). However, these rate constants are obtained at high temperatures (298–753 K) and high pressures (100–600 Torr helium), which are far from the conditions typical for prestellar cores. Our updated model demonstrates results similar to the observational ones without including this reaction; therefore, we removed it. We also switched off the reaction $\text{gN} + \text{gCH}_2\text{OH} \rightarrow \text{gNH}_2\text{CHO}$; although it is present in KIDA (V. Wakelam et al. 2012) with the note that it was listed in the Ohio State University (OSU) gas-grain code from Eric Herbst group in 2006, this seems to be an inefficient way of producing formamide in the solid-state because of the differences in chemical structure of CH_2OH and NH_2CHO . For the reaction $\text{NH}_2 + \text{H}_2\text{CO} \rightarrow \text{NH}_2\text{CHO} + \text{H}$, A. I. Vasyunin et al. (2017) exploit the rates provided by D. Skouteris et al. (2017). However, in a more recent work, K. M. Douglas et al. (2022) suggested that below 110 K the branching ratio for this channel is effectively zero. Thus, under the conditions of the prestellar core characterized by low dust and gas temperatures, we switched this reaction off.

Important surface formation routes for methyl formate (HCOOCH_3), dimethyl ether (CH_3OCH_3), and acetaldehyde

Table 7
Solid Methanol Formation Chemistry

Reaction	Bar. (Å)	E_{act} (K)
$\text{gH} + \text{gCO} \rightarrow \text{gHCO}$	1.35	2320
$\text{gH} + \text{gHCO} \rightarrow \text{gH}_2\text{CO}$	1.00	0
$\text{gH} + \text{gH}_2\text{CO} \rightarrow \text{gCH}_2\text{OH}$	1.35	4500
$\text{gH} + \text{gH}_2\text{CO} \rightarrow \text{gCH}_3\text{O}$	1.35	2320
$\text{gH} + \text{gCH}_2\text{OH} \rightarrow \text{gCH}_3\text{OH}$	1.00	0
$\text{gH} + \text{gCH}_3\text{O} \rightarrow \text{gCH}_3\text{OH}$	1.00	0
$\text{gH} + \text{gHCO} \rightarrow \text{gCO} + \text{gH}_2$	1.00	0
$\text{gH} + \text{gH}_2\text{CO} \rightarrow \text{gHCO} + \text{gH}_2$	1.22	2960
$\text{gH} + \text{gCH}_2\text{OH} \rightarrow \text{gH}_2\text{CO} + \text{gH}_2$	1.00	0
$\text{gH} + \text{gCH}_3\text{O} \rightarrow \text{gH}_2\text{CO} + \text{gH}_2$	1.00	0
$\text{gH} + \text{gCH}_3\text{OH} \rightarrow \text{gCH}_2\text{OH} + \text{gH}_2$	1.00	4380
$\text{gH} + \text{gCH}_3\text{OH} \rightarrow \text{gCH}_3\text{O} + \text{gH}_2$	1.00	6640
$\text{gCH}_3\text{O} + \text{gH}_2\text{CO} \rightarrow \text{gCH}_3\text{OH} + \text{gHCO}$...	2670 ^a
$\text{gCH}_3\text{O} + \text{gCH}_3\text{O} \rightarrow \text{gCH}_3\text{OH} + \text{gH}_2\text{CO}$...	0
$\text{gC} + \text{gH}_2\text{O} \rightarrow \text{gH}_2\text{CO}$...	0 ^{b,c}

Notes. Parameters for hydrogen addition/abstraction reactions are taken from M. Jin & R. T. Garrod (2020).

^a S. Álvarez-Barcia et al. (2018).

^b G. Molpeceres et al. (2021).

^c Also see Appendix B.

Table 8
Acetaldehyde Formation Route (G. Fedoseev et al. 2022)

Reaction	E_{act} (K)
$\text{gC} + \text{gCO} \rightarrow \text{gCCO}$	0 ^a
$\text{gH} + \text{gCCO} \rightarrow \text{gHC}_2\text{O}$	0
$\text{gH} + \text{gHC}_2\text{O} \rightarrow \text{gCH}_2\text{CO}$	0
$\text{gH} + \text{gCH}_2\text{CO} \rightarrow \text{gCH}_3\text{CO}$	975 ^b
$\text{gH} + \text{gCH}_3\text{CO} \rightarrow \text{gCH}_3\text{CHO}$	0

Notes.

^a A. Papakondylis & A. Mavridis (2019).

^b H. Umemoto et al. (1984).

(CH_3CHO) in our nondiffusive model are radical–radical reactions $\text{HCO} + \text{CH}_3\text{O} \rightarrow \text{HCOOCH}_3$, $\text{CH}_3 + \text{CH}_3\text{O} \rightarrow \text{CH}_3\text{OCH}_3$, and $\text{CH}_3 + \text{HCO} \rightarrow \text{CH}_3\text{CHO}$ (M. Allen & G. W. Robinson 1977), although the possibility of other products for the last reaction was also reported (T. Lamberts et al. 2019). Following M. Jin & R. T. Garrod (2020), we also added H-addition/abstraction loops for those species. We included these loops in our network with the barriers for H-abstraction reactions taken from R. T. Garrod (2013) and M. Jin & R. T. Garrod (2020; Table 9); see also S. Álvarez-Barcia et al. (2018) for more details. H-addition reactions forming these species are barrierless. The loops may be important as iterative attempts to desorb a species that result in a net increase of RD probability.

T. Lamberts et al. (2022) showed that, along with reactions with H (D. Qasim et al. 2020), reactions with H_2 are also important for the hydrogenation of carbon atoms into methane on grain surfaces. We updated our reaction barriers according to their results (see Table 10). As for the reaction $\text{gC} + \text{gH}_2 \rightarrow \text{gCH}_2$, T. Lamberts et al. (2022) point out that its activation energy strongly depends on the neighborhood of a binding site of the carbon atom. We have chosen the minimal

Table 9
H-abstraction Reactions for COMs

Reaction	E_{act} (K)
$\text{gH} + \text{gCH}_3\text{CHO} \rightarrow \text{gH}_2 + \text{gCH}_3\text{CO}$	2120 ^{a,b}
$\text{gH} + \text{gCH}_3\text{OCH}_3 \rightarrow \text{gCH}_3\text{OCH}_2 + \text{gH}_2$	4450 ^{c,d}
$\text{gH} + \text{gHCOOCH}_3 \rightarrow \text{gH}_2 + \text{gCH}_3\text{OCO}$	3970 ^{a,e}

Notes.

^a R. T. Garrod (2013).

^b J. Warnatz (1984).

^c M. Jin & R. T. Garrod (2020).

^d K. Takahashi et al. (2007).

^e D. A. Good & J. S. Francisco (2002).

Table 10
Grain-surface Methane Formation Routes (T. Lamberts et al. 2022)

Reaction	E_{act} (K)
$\text{gC} + \text{gH} \rightarrow \text{gCH}$	0
$\text{gCH} + \text{gH} \rightarrow \text{gCH}_2$	0
$\text{gCH}_2 + \text{gH} \rightarrow \text{gCH}_3$	0
$\text{gCH}_3 + \text{gH} \rightarrow \text{gCH}_4$	0
$\text{gC} + \text{gH}_2 \rightarrow \text{gCH}_2$	3600
$\text{gCH} + \text{gH}_2 \rightarrow \text{gCH}_3$	0
$\text{gCH}_2 + \text{gH}_2 \rightarrow \text{gCH}_3 + \text{H}$	5900
$\text{gCH}_3 + \text{gH}_2 \rightarrow \text{gCH}_4 + \text{H}$	5300

activation energy provided by T. Lamberts et al. (2022) equal to 30 kJ mol^{-1} (3600 K).

In previous models of COM formation in cold clouds, the gas-phase reaction of radiative association between CH_3 and CH_3O leading to dimethyl ether ($\text{CH}_3 + \text{CH}_3\text{O} \rightarrow \text{CH}_3\text{OCH}_3$) was shown to play a key role (N. Balucani et al. 2015; A. I. Vasyunin et al. 2017). Rates of reactions of radiative association are known poorly. In N. Balucani et al. (2015) and A. I. Vasyunin et al. (2017), the rate of this reaction at 10 K was taken equal to $3 \times 10^{-10} \text{ cm}^3 \text{ s}^{-1}$. Recently, J. Tennis et al. (2021) studied the gas-phase formation path for dimethyl ether by the radiative association of CH_3 and CH_3O radicals. They calculated the rate coefficient by two methods, canonical and phase-space, and provided the rate constants for modified Arrhenius rate expressions. We adopted the rate constant obtained by the phase-space method, as J. Tennis et al. (2021) report it to be more precise. The Arrhenius coefficients for the rate are $\alpha = 1.37 \times 10^{-12} \text{ cm}^3 \text{ s}^{-1}$, $\beta = -0.96$, $\gamma = 0.00$. This gives a rate constant of the reaction at 10 K equal to $3.6 \times 10^{-11} \text{ cm}^3 \text{ s}^{-1}$, which is almost an order of magnitude lower than the values used previously.

Binding energies of species utilized in this study are the same as in I. Jiménez-Serra et al. (2021) with exception for molecular hydrogen H_2 and atomic carbon. For molecular hydrogen, we adopted the value of binding energy equal to 380 K, which is closer to the estimate provided in M. Minissale et al. (2022). The binding energy of atomic carbon was taken equal to 10,000 K (V. Wakelam et al. 2017). Such a high value reflects the fact that carbon atoms can be partially chemisorbed on amorphous H_2O ice. In this work, we do not use systematically the values of binding energies and preexponential factors of surface species presented in M. Minissale et al. (2022). In a narrow range of grain temperatures that

exists in our model of L1544 (7–15 K), those new factors combined with accordingly adjusted binding energies introduce very little changes to the chemistry calculated using values utilized in I. Jiménez-Serra et al. (2021).

Appendix C Diffusive Model

C.1. Agreement with Observations

To find out the role of nondiffusive grain chemistry for COM formation in comparison with other processes, we also run a model with the same set of parameters and GRD chemical desorption, but the nondiffusive reactions switched off. This model is in the following referred to as the diffusive model. Like in the case of our GRD model, we created agreement maps to compare our modeling data with the observational data (Figure 11). At the central area of the core, the modeled abundances fit the observational data only in a narrow time interval from 2×10^4 to 4×10^4 yr, which is not suitable for us because CO is not depleted yet. The direct comparison with Figure 3 shows that the nondiffusive model demonstrates a wider range of “agreement” over the chosen parameter space. Therefore, we provide the results for the diffusive model at the time point of 10^5 yr to perform a reasonable comparison with our GRD model.

In the case of our diffusive model, almost all species of our interest demonstrate the modeling abundances *in agreement* (in the sense of the definition given in Section 3.2) with the observational results for gaseous COMs (Figure 12, top panel). The exception is HCOOCH_3 , whose modeled abundance is more than an order of magnitude lower than the observational one. However, when taking into account observational errors, this difference does not look crucial. It is also worth noting that CH_3O modeled abundance does not show a peak in our diffusive model. Nevertheless, the agreement with the observational results is still reasonable. The abundances of the main ice components are also reasonable except CO_2 (which is produced via the nondiffusive processes in our GRD model), and ice COMs practically disappear in the central parts of the core (Figure 12, middle and bottom panels).

C.2. Chemistry at the Methanol Peak for the Diffusive Model

We describe the chemistry of COMs at the position of the methanol peak in our diffusive model. All values are given for the time moment of $\approx 10^5$ yr.

CH_3OH . Like in our GRD model, the H-addition reactions are the major paths to the adsorbed species constituting the methanol formation chain (Table 7). The exception is CH_2OH ice, produced by the H-abstraction reaction from CH_3OH .

HCOOCH_3 . In our diffusive model, the only efficient channel of methyl formate production is the gas-phase reaction $\text{CH}_3\text{OCH}_2 + \text{O} \rightarrow \text{HCOOCH}_3 + \text{H}$ (N. Balucani et al. 2015). The predominant source of CH_3OCH_2 radical is RD in the reaction $\text{gCH}_2 + \text{gCH}_3\text{O} \rightarrow \text{gCH}_3\text{OCH}_2$ (M. Jin & R. T. Garrod 2020). In contrast to the position of the dust peak, this reaction has a nonnegligible rate at the position of the observed methanol peak. As in our GRD model, switching off the reaction $\text{CH}_3\text{OH}_2^+ + \text{HCOOH} \rightarrow \text{HC(OH)OCH}_3^+ + \text{H}_2\text{O}$ in our diffusive model does not affect HCOOCH_3 abundance. In the absence of nondiffusive processes, RD following the surface reactions $\text{gH} + \text{gCH}_3\text{OCO} \rightarrow \text{gHCOOCH}_3$ and $\text{gHCO} +$

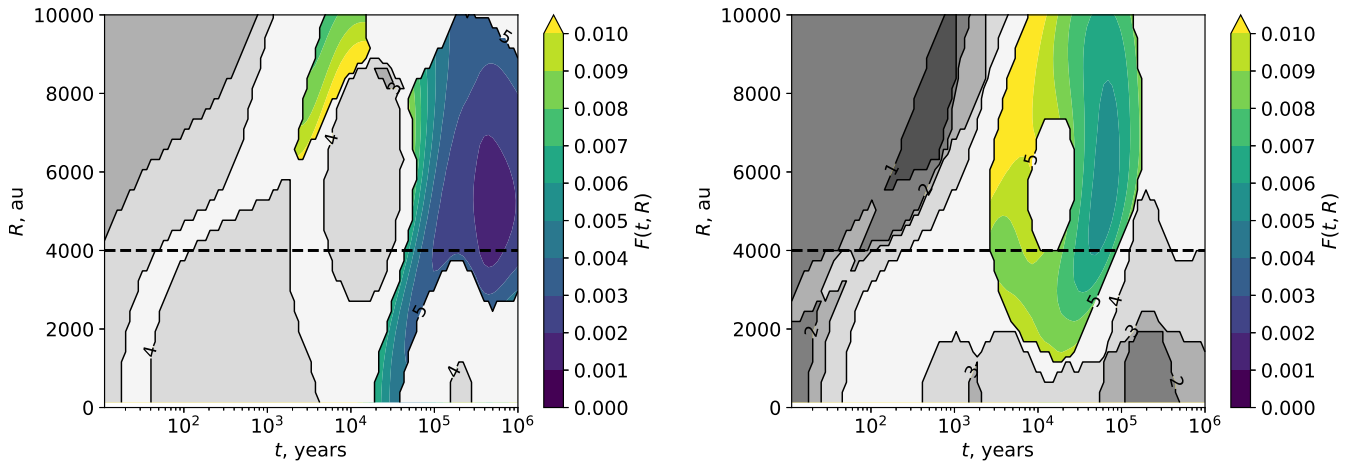


Figure 11. Agreement maps for the dust peak (left) and for the methanol peak (right), the diffusive model. The details are the same as in Figure 3.

$\text{gCH}_3\text{O} \rightarrow \text{gHCOOCH}_3$ provides less than 1% of gaseous methyl formate abundance.

CH_3CHO . The reaction $\text{gH} + \text{gCH}_3\text{CO} \rightarrow \text{gCH}_3\text{CHO}$ accounts for almost all dust-to-gas CH_3CHO transfer rate and for 84% of gaseous acetaldehyde production. Gas-phase processes accounting for the rest of acetaldehyde formation rate are the dissociative recombination of protonated acetaldehyde $(\text{CH}_3\text{CHO})\text{H}^+$ and the reaction $\text{O} + \text{C}_2\text{H}_5 \rightarrow \text{CH}_3\text{CHO} + \text{H}$. As for $(\text{CH}_3\text{CHO})\text{H}^+$, 55% of its formation rate is due to the reactions $\text{H}_3\text{O}^+ + \text{C}_2\text{H}_2 \rightarrow (\text{CH}_3\text{CHO})\text{H}^+$ and $\text{H}_2\text{CO}^+ + \text{CH}_4 \rightarrow (\text{CH}_3\text{CHO})\text{H}^+ + \text{H}$, and the rest is due to the loops including the reactions of acetaldehyde with H_3^+ , HCO^+ or H_3O^+ .

Surface acetaldehyde is the end species in the chain of hydrogenation reactions $\text{gHC}_2\text{O} \rightarrow \text{gCH}_2\text{CO} \rightarrow \text{gCH}_3\text{CO} \rightarrow \text{gCH}_3\text{CHO}$. Thus, similarly to our GRD model, here, we find a part of the acetaldehyde ice production path described in G. Fedoseev et al. (2022) and S. Ferrero et al. (2023). Importantly, at the position of the methanol peak, gHC_2O predominantly accretes from gas—the efficiency of the reaction $\text{gH} + \text{gCCO} \rightarrow \text{gHC}_2\text{O}$ is very low because of low CCO abundance. Toward the edge of the core, at a distance of ≈ 20000 au, the reaction $\text{gC} + \text{gCO} \rightarrow \text{gCCO}$ proceeds efficiently even in a diffusive mode, which enhances surface acetaldehyde production and therefore its dust-to-gas desorption rate. At large radii, gas-phase acetaldehyde abundance becomes even greater than methanol gas-phase abundance.

CH_3OCH_3 . The H-addition surface reaction $\text{gH} + \text{gCH}_3\text{OCH}_2 \rightarrow \text{gCH}_3\text{OCH}_3$ is the predominant source of gaseous CH_3OCH_3 via RD and also the major source of dimethyl ether ice. The radical gCH_3OCH_2 is produced via the reaction $\text{gCH}_2 + \text{gCH}_3\text{O} \rightarrow \text{gCH}_3\text{OCH}_2$.

Gas-phase reactions practically do not contribute to the production of CH_3OCH_3 . The only noticeable process is the dissociative recombination of protonated dimethyl ether $(\text{CH}_3)_2\text{OH}^+$, which is predominantly produced in loops via the reactions of dimethyl ether with H_3^+ , HCO^+ , and H_3O^+ . Only 8% of $(\text{CH}_3)_2\text{OH}^+$ is a product of the reaction $\text{CH}_3^+ + \text{CH}_3\text{OH} \rightarrow (\text{CH}_3)_2\text{OH}^+$.

NH_2CHO . Due to the lack of nondiffusive mechanisms, the reaction $\text{gNH}_2 + \text{gHCO} \rightarrow \text{gNH}_2\text{CHO}$ responsible for formamide formation on the grain surface appears to be slow.

Since we switch the gas-phase reaction of NH_2 and H_2CO off under the conditions of the prestellar core (K. M. Douglas et al. 2022), gaseous formamide has no efficient production paths and demonstrates an abundance of $\sim 10^{-14}$ at the position of the methanol peak.

C.3. Issues of the Diffusive Model and Possible Indicators for Nondiffusive Mechanisms Efficiency

The only efficient process supplying gaseous methyl formate and dimethyl ether in our diffusive model is the reaction $\text{gCH}_2 + \text{gCH}_3\text{O} \rightarrow \text{gCH}_3\text{OCH}_2$. At the methanol peak with the dust temperature ~ 10 K, it proceeds efficiently even in the diffusive mode. When switching it off, the HCOOCH_3 and CH_3OCH_3 calculated gas-phase abundances drop by about 2 orders of magnitude at the methanol peak position. In our reactions network, CH_2 has a desorption energy of 1050 K; however, higher values exist. KIDA astrochemical database provides 1400 K as the desorption energy for CH_2 (V. Wakelam et al. 2017). When we incorporate this value in our network, the gas-phase abundances of methyl formate and dimethyl ether drop by some tenths of an order of magnitude.

Creating the diagram for the diffusive model as the one in Figure 9 shows that the model provides abundances for all the studied gaseous COMs in agreement with the observations only in a very narrow range of $E_{\text{diff}}/E_{\text{des}} = 0.55\text{--}0.60$ for atomic species and $E_{\text{diff}}/E_{\text{des}} = 0.30$ for molecular species. At these parameters, ice composition does not look reasonable, with too high abundances of atomic H and free radicals.

Going back to the diffusive model with our default parameters ($E_{\text{diff}}/E_{\text{des}} = 0.50$ for atomic species and 0.30 for molecular ones), we find the abundance of CO_2 ice dropping to 10^{-7} in the absence of nondiffusive processes. Other main ice components do not demonstrate significant variations in abundance between the nondiffusive and diffusive models. In our GRD model, CO_2 ice is a product of nondiffusive processes; however, there exist ways to obtain relevant CO_2 ice abundance other than implementing nondiffusive reactions—for example, changing physical conditions during the translucent cloud phase. Being formed during the “precore” phase, CO_2 ice may survive in the central area of the core in the absence of strong photolysis or radiolysis. Interestingly, A. Clément et al. (2023) in their simulations produce

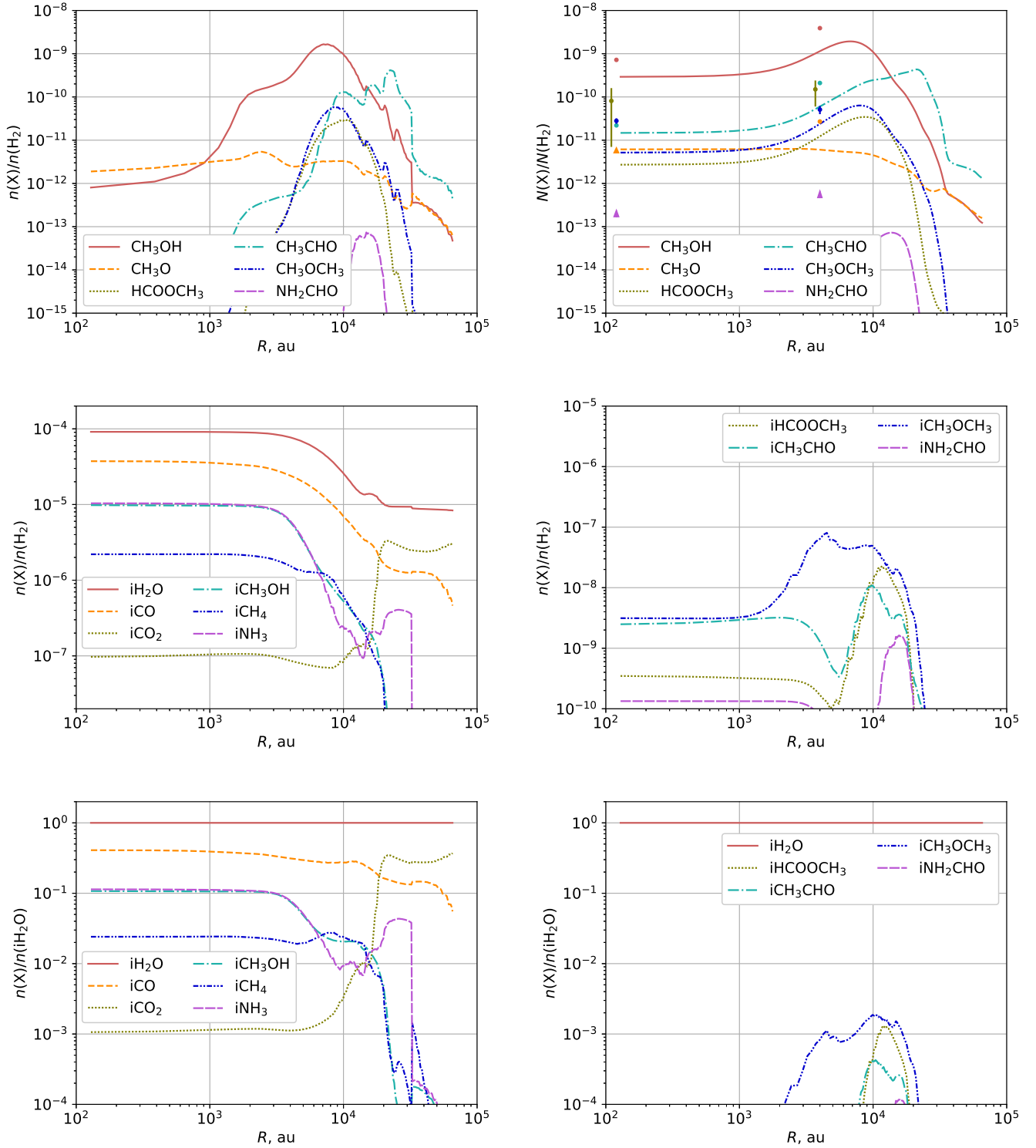


Figure 12. Radial profiles obtained with our diffusive model at 10^5 yr. Top: profiles of modeled abundances (top left) and abundances derived as column density ratios (top right) of complex organic species. Abundances derived as column densities are smoothed over the $26''$ Gaussian beam. Middle: profiles of abundances of major ice constituents (middle left) and selected complex organic molecules in the ice (middle right) w.r.t. H_2 . Bottom: same as in the middle, but w.r.t. H_2O . Colored dots in the top right panel denote observational values by A. Chacón-Tanarro et al. (2019) for CH_3OH and by I. Jiménez-Serra et al. (2016) for other species, vertical lines are for error bars, and arrows are for observational upper limits.

significant amounts of CO_2 ice at 10 K without invoking nondiffusive chemistry. Their main gCO_2 formation route is $gCO + gO$, with the older binding energy value of 800 K assumed for atomic oxygen instead of 1660 K.

Since both diffusive and GRD models provide reasonable gaseous COM abundances (except for methyl formate in the diffusive model), it is good to have some indicator species in addition to CO_2 whose observational abundances may help to

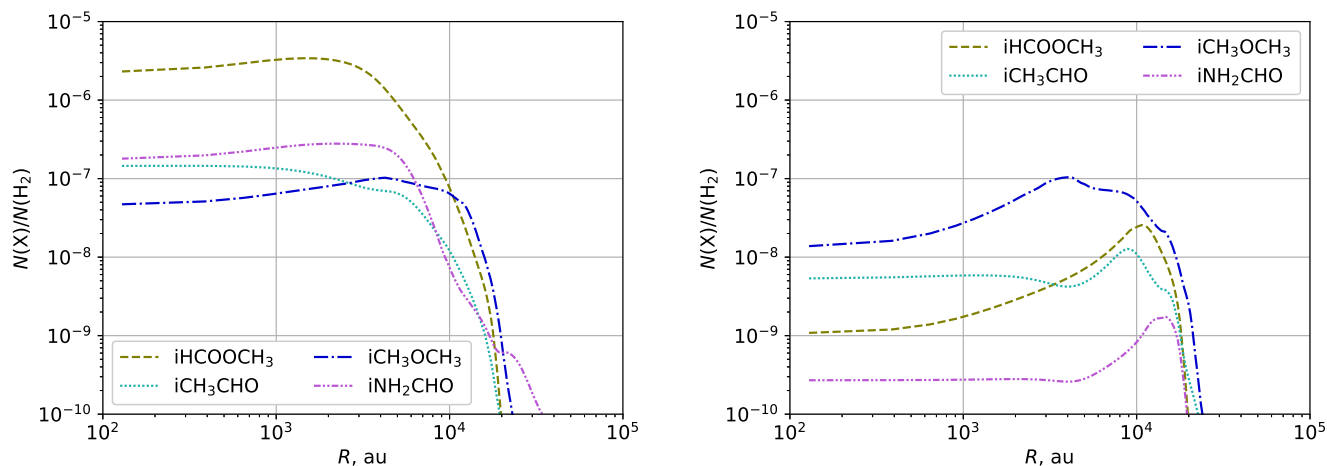


Figure 13. Comparison of ice COM abundances derived as column densities ratios (not smoothed over a beam in this case) for the GRD model (left) and the diffusive model (right).

learn if nondiffusive processes do have a significant effect on ice chemistry. The comparison of ice COM abundances derived from column densities (Figure 13) shows that, at the central area of the core, CH_3OCH_3 ice abundance differs no more than an order of magnitude between the diffusive and GRD models, but other ice COMs demonstrate much larger variations in abundance: more than 1 order of magnitude for CH_3CHO , more than 2 orders of magnitude for NH_2CHO , and more than 3 orders of magnitude for HCOOCH_3 . Future ice composition observations with JWST may help to find out which type of processes dominates ice chemistry.

ORCID iDs

Katerina Borshcheva <https://orcid.org/0000-0001-5618-4660>
 Gleb Fedoseev <https://orcid.org/0000-0003-2434-2219>
 Anna F. Punanova <https://orcid.org/0000-0001-6004-875X>
 Paola Caselli <https://orcid.org/0000-0003-1481-7911>
 Izaskun Jiménez-Serra <https://orcid.org/0000-0003-4493-8714>
 Anton I. Vasyunin <https://orcid.org/0000-0003-1684-3355>

References

- Acharyya, K. 2014, *MNRAS*, 443, 1301
 Acharyya, K. 2022, *PASA*, 39, e009
 Al-Halabi, A., & van Dishoeck, E. F. 2007, *MNRAS*, 382, 1648
 Allen, M., & Robinson, G. W. 1977, *ApJ*, 212, 396
 Álvarez-Barcia, S., Russ, P., Kästner, J., & Lamberts, T. 2018, *MNRAS*, 479, 2007
 Bacmann, A., & Faure, A. 2016, *A&A*, 587, A130
 Bacmann, A., Taquet, V., Faure, A., Kahane, C., & Ceccarelli, C. 2012, *A&A*, 541, L12
 Balucani, N., Ceccarelli, C., & Taquet, V. 2015, *MNRAS*, 449, L16
 Barone, V., Latouche, C., Skouteris, D., et al. 2015, *MNRAS*, 453, L31
 Bergner, J. B., Öberg, K. I., & Rajappan, M. 2017, *ApJ*, 845, 29
 Bertin, M., Romanzin, C., Doronin, M., et al. 2016, *ApJL*, 817, L12
 Bianchi, E., Codella, C., Ceccarelli, C., et al. 2019, *MNRAS*, 483, 1850
 Bisschop, S. E., Fraser, H. J., Öberg, K. I., van Dishoeck, E. F., & Schlemmer, S. 2006, *A&A*, 449, 1297
 Bizzocchi, L., Caselli, P., Spezzano, S., & Leonardo, E. 2014, *A&A*, 569, A27
 Boogert, A. C. A., Gerakines, P. A., & Whittet, D. C. B. 2015, *ARA&A*, 53, 541
 Bottinelli, S., Ceccarelli, C., Lefloch, B., et al. 2004, *ApJ*, 615, 354
 Bottinelli, S., Ceccarelli, C., Williams, J. P., & Lefloch, B. 2007, *A&A*, 463, 601
 Buch, V., & Zhang, Q. 1991, *ApJ*, 379, 647
 Butscher, T., Duvernay, F., Danger, G., & Chiavassa, T. 2016, *A&A*, 593, A60
 Caselli, P., Pineda, J. E., Sipilä, O., et al. 2022, *ApJ*, 929, 13
 Caselli, P., Pineda, J. E., Zhao, B., et al. 2019, *ApJ*, 874, 89
 Caselli, P., Walmsley, C. M., Tafalla, M., Dore, L., & Myers, P. C. 1999, *ApJL*, 523, L165
 Cazaux, S., Minissale, M., Dulieu, F., & Hocuk, S. 2016, *A&A*, 585, A55
 Cazaux, S., Morisset, S., Spaans, M., & Allouche, A. 2011, *A&A*, 535, A27
 Cazaux, S., Tielens, A. G. G. M., Ceccarelli, C., et al. 2003, *ApJL*, 593, L51
 Cernicharo, J., Marcelino, N., Roueff, E., et al. 2012, *ApJL*, 759, L43
 Chacón-Tanarro, A., Caselli, P., Bizzocchi, L., et al. 2019, *A&A*, 622, A141
 Chuang, K. J., Fedoseev, G., Qasim, D., et al. 2018, *ApJ*, 853, 102
 Chuang, K. J., Jäger, C., Krasnokutski, S. A., Fulvio, D., & Henning, T. 2022, *ApJ*, 933, 107
 Clément, A., Taillard, A., Wakelam, V., et al. 2023, *A&A*, 675, A165
 Crapsi, A., Caselli, P., Walmsley, C. M., et al. 2005, *ApJ*, 619, 379
 Crapsi, A., Caselli, P., Walmsley, M. C., & Tafalla, M. 2007, *A&A*, 470, 221
 Cruz-Díaz, G. A., Martín-Doménech, R., Muñoz Caro, G. M., & Chen, Y. J. 2016, *A&A*, 592, A68
 Cuppen, H. M., van Dishoeck, E. F., Herbst, E., & Tielens, A. G. G. M. 2009, *A&A*, 508, 275
 Cuppen, H. M., Walsh, C., Lamberts, T., et al. 2017, *SSRv*, 212, 1
 Dartois, E., Chabot, M., Bacmann, A., et al. 2020, *A&A*, 634, A103
 Dartois, E., Chabot, M., Id Barkach, T., et al. 2018, *A&A*, 618, A173
 Dartois, E., Chabot, M., Id Barkach, T., et al. 2021, *A&A*, 647, A177
 Dartois, E., Noble, J. A., Caselli, P., et al. 2024, *NatAs*, 8, 359
 Douglas, K. M., Lucas, D. I., Walsh, C., et al. 2022, *ApJL*, 937, L16
 Fayolle, E. C., Bertin, M., Romanzin, C., et al. 2011, *ApJL*, 739, L36
 Fedoseev, G., Chuang, K. J., van Dishoeck, E. F., Ioppolo, S., & Linnartz, H. 2016, *MNRAS*, 460, 4297
 Fedoseev, G., Cuppen, H. M., Ioppolo, S., Lamberts, T., & Linnartz, H. 2015, *MNRAS*, 448, 1288
 Fedoseev, G., Qasim, D., Chuang, K.-J., et al. 2022, *ApJ*, 924, 110
 Fedoseev, G., Scirè, C., Baratta, G. A., & Palumbo, M. E. 2018, *MNRAS*, 475, 1819
 Ferrero, S., Ceccarelli, C., Ugliengo, P., Sodupe, M., & Rimola, A. 2023, *ApJ*, 951, 150
 Fredon, A., & Cuppen, H. M. 2018, *PCCP*, 20, 5569
 Fredon, A., Radchenko, A. K., & Cuppen, H. M. 2021, *Acc. Chem. Res.*, 54, 745
 Fuchs, G. W., Acharyya, K., Bisschop, S. E., et al. 2006, *FaDi*, 133, 331
 Fuchs, G. W., Cuppen, H. M., Ioppolo, S., et al. 2009, *A&A*, 505, 629
 Furuya, K. 2024, *ApJ*, 974, 115
 Furuya, K., Hama, T., Oba, Y., et al. 2022, *ApJL*, 933, L16
 Furuya, K., Oba, Y., & Shimonishi, T. 2022, *ApJ*, 926, 171
 Garrod, R., Park, I. H., Caselli, P., & Herbst, E. 2006, *FaDi*, 133, 51
 Garrod, R. T. 2008, *A&A*, 491, 239
 Garrod, R. T. 2013, *ApJ*, 765, 60
 Garrod, R. T., Belloche, A., Müller, H. S. P., & Menten, K. M. 2017, *A&A*, 601, A48
 Garrod, R. T., & Herbst, E. 2006, *A&A*, 457, 927
 Garrod, R. T., Jin, M., Matis, K. A., et al. 2022, *ApJS*, 259, 1
 Garrod, R. T., & Pauly, T. 2011, *ApJ*, 735, 15

- Garrod, R. T., Vasyunin, A. I., Semenov, D. A., Wiebe, D. S., & Henning, T. 2009, *ApJL*, **700**, L43
- Garrod, R. T., Wakelam, V., & Herbst, E. 2007, *A&A*, **467**, 1103
- Garrod, R. T., Weaver, W. S. L., & Herbst, E. 2008, *ApJ*, **682**, 283
- Gieser, C., Semenov, D., Beuther, H., et al. 2019, *A&A*, **631**, A142
- Good, D. A., & Francisco, J. S. 2002, *JPCA*, **106**, 1733
- Goto, M., Vasyunin, A. I., Giuliano, B. M., et al. 2021, *A&A*, **651**, A53
- Grassi, T., Bovino, S., Caselli, P., et al. 2020, *A&A*, **643**, A155
- Hama, T., Kuwahata, K., Watanabe, N., et al. 2012, *ApJ*, **757**, 185
- Hama, T., & Watanabe, N. 2013, *ChRv*, **113**, 8783
- Hasegawa, T. I., & Herbst, E. 1993, *MNRAS*, **261**, 83
- Hasegawa, T. I., Herbst, E., & Leung, C. M. 1992, *ApJS*, **82**, 167
- He, J., Acharyya, K., & Vidali, G. 2016a, *ApJ*, **825**, 89
- He, J., Acharyya, K., & Vidali, G. 2016b, *ApJ*, **823**, 56
- Herbst, E., & van Dishoeck, E. F. 2009, *ARA&A*, **47**, 427
- Hollenbach, D., & McKee, C. F. 1979, *ApJS*, **41**, 555
- Hollenbach, D., & Salpeter, E. E. 1970, *JChPh*, **53**, 79
- Ikeda, M., Ohishi, M., Nummelin, A., et al. 2001, *ApJ*, **560**, 792
- Ioppolo, S., Fedoseev, G., Chuang, K. J., et al. 2021, *NatAs*, **5**, 197
- Ivlev, A. V., Giuliano, B. M., Juhász, Z., et al. 2023, *ApJ*, **944**, 181
- Jiménez-Serra, I., Vasyunin, A. I., Caselli, P., et al. 2016, *ApJL*, **830**, L6
- Jiménez-Serra, I., Vasyunin, A. I., Spezzano, S., et al. 2021, *ApJ*, **917**, 44
- Jin, M., & Garrod, R. T. 2020, *ApJS*, **249**, 26
- Jin, M., Lam, K. H., McClure, M. K., et al. 2022, *ApJ*, **935**, 133
- Johnson, D. G., Blitz, M. A., & Seakins, P. W. 2000, *PCCP*, **2**, 2549
- Jones, A. P., & Williams, D. A. 1985, *MNRAS*, **217**, 413
- Jørgensen, J. K., Müller, H. S. P., Calcutt, H., et al. 2018, *A&A*, **620**, A170
- Kalvans, J. 2018, *MNRAS*, **478**, 2753
- Karssemeijer, L. J., & Cuppen, H. M. 2014, *A&A*, **569**, A107
- Keto, E., & Caselli, P. 2008, *ApJ*, **683**, 238
- Keto, E., & Caselli, P. 2010, *MNRAS*, **402**, 1625
- Kuwahata, K., Hama, T., Kouchi, A., & Watanabe, N. 2015, *PhRvL*, **115**, 133201
- Lamberts, T., Fedoseev, G., van Hemert, M. C., et al. 2022, *ApJ*, **928**, 48
- Lamberts, T., Markmeyer, M. N., Kolb, F. J., & Kästner, J. 2019, *ESC*, **3**, 958
- Lattanzi, V., Bizzocchi, L., Vasyunin, A. I., et al. 2020, *A&A*, **633**, A118
- Lee, J.-E., Baek, G., Lee, S., et al. 2023, *ApJ*, **956**, 43
- Li, J., & Guo, H. 2014, *PCCP*, **16**, 6753
- López-Sepulcre, A., Sakai, N., Neri, R., et al. 2017, *A&A*, **606**, A121
- Marcelino, N., Cernicharo, J., Agúndez, M., et al. 2007, *ApJL*, **665**, L127
- Masuda, K., & Takahashi, J. 1997, *AdSpR*, **19**, 1019
- Matar, E., Bergeron, H., Dulieu, F., et al. 2010, *JChPh*, **133**, 104507
- McClure, M. K., Rocha, W. R. M., Pontoppidan, K. M., et al. 2023, *NatAs*, **7**, 431
- Megías, A., Jiménez-Serra, I., Martín-Pintado, J., et al. 2023, *MNRAS*, **519**, 1601
- Minissale, M., Aikawa, Y., Bergin, E., et al. 2022, *ESC*, **6**, 597
- Minissale, M., Congiu, E., & Dulieu, F. 2016a, *A&A*, **585**, A146
- Minissale, M., & Dulieu, F. 2014, *JChPh*, **141**, 014304
- Minissale, M., Dulieu, F., Cazaux, S., & Hocuk, S. 2016b, *A&A*, **585**, A24
- Molpeceres, G., Kästner, J., Fedoseev, G., et al. 2021, *J. Phys. Chem. Lett.*, **12**, 44
- Nagy, Z., Spezzano, S., Caselli, P., et al. 2019, *A&A*, **630**, A136
- Oba, Y., Tomaru, T., Lamberts, T., Kouchi, A., & Watanabe, N. 2018, *NatAs*, **2**, 228
- Oba, Y., Watanabe, N., Hama, T., et al. 2012, *ApJ*, **749**, 67
- Oberg, K. I. 2016, *Chem. Rev.*, **116**, 9631
- Öberg, K. I., Boogert, A. C. A., Pontoppidan, K. M., et al. 2011, *ApJ*, **740**, 109
- Öberg, K. I., van Broekhuizen, F., Fraser, H. J., et al. 2005, *ApJL*, **621**, L33
- Paardekooper, D. M., Bossa, J. B., & Linnartz, H. 2016, *A&A*, **592**, A67
- Papakondylis, A., & Mavridis, A. 2019, *JPCA*, **123**, 10290
- Pilling, S., Seperuelo Duarte, E., da Silveira, E. F., et al. 2010, *A&A*, **509**, A87
- Prasad, S. S., & Tarafdar, S. P. 1983, *ApJ*, **267**, 603
- Punanova, A., Caselli, P., Feng, S., et al. 2018, *ApJ*, **855**, 112
- Punanova, A., Vasyunin, A., Caselli, P., et al. 2022, *ApJ*, **927**, 213
- Qasim, D., Fedoseev, G., Chuang, K. J., et al. 2020, *NatAs*, **4**, 781
- Qasim, D., Lamberts, T., He, J., et al. 2019, *A&A*, **626**, A118
- Redaelli, E., Chacón-Tanarro, A., Caselli, P., et al. 2022, *ApJ*, **941**, 168
- Riedel, W., Sipilä, O., Redaelli, E., et al. 2023, *A&A*, **680**, A87
- Ruud, M., Loison, J. C., Hickson, K. M., et al. 2015, *MNRAS*, **447**, 4004
- Ruud, M., Wakelam, V., & Hersant, F. 2016, *MNRAS*, **459**, 3756
- Ruffe, D. P., & Herbst, E. 2000, *MNRAS*, **319**, 837
- Santos, J. C., Chuang, K.-J., Lamberts, T., et al. 2022, *ApJL*, **931**, L33
- Santos, J. C., Linnartz, H., & Chuang, K. J. 2023, *A&A*, **678**, A112
- Scibelli, S., Shirley, Y., Megías, A., & Jiménez-Serra, I. 2024, *MNRAS*, **533**, A104
- Scibelli, S., Shirley, Y., Vasyunin, A., & Launhardt, R. 2021, *MNRAS*, **504**, 5754
- Senevirathne, B., Andersson, S., Dulieu, F., & Nyman, G. 2017, *MolAs*, **6**, 59
- Shingledecker, C. N., Lamberts, T., Laas, J. C., et al. 2020, *ApJ*, **888**, 52
- Shingledecker, C. N., Tennis, J., Le Gal, R., & Herbst, E. 2018, *ApJ*, **861**, 20
- Shingledecker, C. N., Vasyunin, A., Herbst, E., & Caselli, P. 2019, *ApJ*, **876**, 140
- Skouteris, D., Balucani, N., Ceccarelli, C., et al. 2018, *ApJ*, **854**, 135
- Skouteris, D., Vazart, F., Ceccarelli, C., et al. 2017, *MNRAS*, **468**, L1
- Song, L., & Kästner, J. 2016, *PCCP*, **18**, 29278
- Spezzano, S., Bizzocchi, L., Caselli, P., Harju, J., & Brünken, S. 2016, *A&A*, **592**, L11
- Sutton, E. C., Peng, R., Danchi, W. C., et al. 1995, *ApJS*, **97**, 455
- Tafalla, M., Myers, P. C., Caselli, P., Walmsley, C. M., & Comito, C. 2002, *ApJ*, **569**, 815
- Takahashi, K., Yamamoto, O., Inomata, T., & Kogoma, M. 2007, *Int. J. Chem. Kinet.*, **39**, 97
- Taquet, V., Wirstrom, E. S., Charnley, S. B., et al. 2017, *A&A*, **607**, A20
- Tennis, J., Loison, J.-C., & Herbst, E. 2021, *ApJ*, **922**, 133
- Umamoto, H., Tsunashima, S., Sato, S., Washida, N., & Hatakeyama, S. 1984, *BCSJ*, **57**, 2578
- Vasyunin, A. I., Caselli, P., Dulieu, F., & Jiménez-Serra, I. 2017, *ApJ*, **842**, 33
- Vasyunin, A. I., & Herbst, E. 2013, *ApJ*, **769**, 34
- Veeraghatham, V. K., Manrodt, K., Lewis, S. P., & Stancil, P. C. 2014, *ApJ*, **790**, 4
- Wakelam, V., Dartois, E., Chabot, M., et al. 2021, *A&A*, **652**, A63
- Wakelam, V., & Herbst, E. 2008, *ApJ*, **680**, 371
- Wakelam, V., Herbst, E., Loison, J. C., et al. 2012, *ApJS*, **199**, 21
- Wakelam, V., Loison, J. C., Mereau, R., & Ruud, M. 2017, *MolAs*, **6**, 22
- Warnatz, J. 1984, *Combustion: Physical and Chemical Fundamentals, Modeling and Simulation, Experiments, Pollutant Formation* (New York: Springer), 209
- Watanabe, N., Kimura, Y., Kouchi, A., et al. 2010, *ApJL*, **714**, L233
- Wirstrom, E. S., Charnley, S. B., Persson, C. M., et al. 2014, *ApJL*, **788**, L32